# Size-Dependent Optical Band Gaps in Metal-Organic Framework Nanoparticles

Faiqa Khaliq,[1] Ryan A. Beck,[2] Erik Svensson Grape,[1] Golnaz Navidi,[1] Miles Griffith,[1] Checkers R. Marshall,[1] Xiaosong Li,[2] and Carl K. Brozek*[1]

[1]*Department of Chemistry and Biochemistry, Materials Science Institute, Oregon Center for Electrochemistry University of Oregon, Eugene, OR 97403, United States*

[2]*Department of Chemistry, University of Washington, Seattle, WA 98195, United States*

Email: cbrozek@uoregon.edu

**Abstract.** Decades of research into size-dependent semiconductor optical gaps have focused on quantum confinement as the dominant mechanism. Emerging reports indicate that lattice strain—intentional or incidental—can impart optical shifts similar or greater in magnitude. Here, we report evidence of optical absorption and photoluminescence spectra of *M*(1,2,3-triazolate)$_2$ *M* = Mg, Cr, Mn, Fe, Co, Cu, Zn, Cd nanoparticles that blueshift from bulk values with decreasing particle sizes in a manner that defies explanation by conventional quantum confinement. The phenomenon persists for particle sizes as large as 200 nm, whereas quantum confinement generally ceases beyond 20-30 nm diameters, and follows a weaker dependence on particle radius. Computational simulations and crystallographic analysis suggest this behavior arises from size-dependent changes to metal-linker bonding that manifests in strain values comparable to literature reports of strain-induced optical shifts in other classes of materials. This behavior appears beyond this family of materials in other notable examples of MOFs, including the well-studied $Cu_3$(trimesate)$_2$ (CuBTC), where smaller sizes correlate with blue-shifted optical gaps. Taken together, these results represent one of the few examples of size-dependent strain in crystalline materials and reinforce the emerging view that MOFs become softer materials when isolated as nanoparticles.

**Introduction**

Photochemistry exemplifies the structure-function relationships of chemical research. All aspects of atomic composition, molecular symmetry, and orbital interactions dictate the optical behavior of molecules, nanomaterials, and extended solids—their optical absorption and photoluminescence intensities, spectral band shapes, and excited-state lifetimes. Defects, interfaces, and surfaces, too, serve as key structural determinants of myriad photophysical processes, from exciton recombination at p-n junctions in light-emitting diodes to charge transfer across the semiconductor-liquid interface during photocatalytic generation of solar fuels. Beyond tuning the composition of molecules and crystalline solids, nanosizing materials has served for decades as an additional synthetic avenue for tuning optical behavior. Quantum confinement,[1,2] plasmonic behavior, the quantum mechanical stark effect,[3–5] and the ability to alter optical behavior through surface-based interfacial redox and molecular dipoles[6,7] all arise from nanoscale structure. Optical band gaps, hereafter termed optical gaps, ($E_{opt}$), serve as useful metrics for evaluating these structure-function relationships.[8–12] They refer to the photon energy required to reach the lowest-energy optically excited state for a molecule or material and relate to the fundamental or HOMO-LUMO gap $E_g$, through the relationship $E_g = E_{opt} + E_b$, where $E_b$ is the exciton binding energy. For instance, careful functionalization of pyridyl iridium photosensitizers adjusts $E_{opt}$ and the photoredox potentials needed for aminoalkylation of alkenes,[13] while down-sizing CdSe diameters from 11 nm to 1.4 nm shifts $E_{opt}$ and band-edge photoluminescence by > 1 eV.[14] Novel synthetic approaches to controlling $E_{opt}$ therefore attract widespread interest.

Recently, we reported that colloidal nanocrystals of the metal-organic framework (MOF) Fe(1,2,3-triazolate)$_2$ (Fe(TA)$_2$) exhibit size-dependent optical behavior that eludes explanation by conventional models such as quantum confinement, or by unintentional effects such as Fe oxidation or change of spin state.[15] Like quantum dots, the $E_{opt}$ of Fe(TA)$_2$ particles blueshift as diameters decrease from bulk sizes to just 6 nm, but $E_{opt}$ follows a much weaker dependence on particle radius. Instead, the effect persists for sizes as large as 150 nm, whereas quantum dots generally reach bulk $E_{opt}$ at diameters around 20 nm.[1,2] Only materials with

exceptionally large dielectric constants and high charge mobilities, such as PbSe, retain size-dependent optical behavior at larger sizes.[16–19] Unlike electrostatic or quantum mechanical interactions that diminish beyond 10-20 nm, crystallite micro-strain is routinely extracted from X-ray scattering data for particles 20-200 nm in size and has been recently shown to shift $E_{opt}$ by at least 100 meV for each 1% increase in micro-strain for various perovskites,[20] binary lattice semiconductors,[21] and 2-D van der Waals sheets.[22,23] To clarify, "micro-strain" refers to a distribution lattice parameters within a material, whereas "strain" typically refers to a set of lattice parameters deviating from a known crystallographic structure. Although long-range micro-strain or any localized geometrical distortion could account shifts to $E_{opt}$, few if any studies have reported that these effects depend on size.

Emerging evidence suggests that metal-linker bonding in MOFs becomes more labile and tolerant to structural distortion as particle sizes decrease. We have argued previously[24] that this behavior may relate, at a fundamental level, to the observation that lattice constants generally increase while phase change critical temperatures decrease as semiconductor particle diameters diminish in size.[25–27] Variable-temperature spectroscopy of common MOF materials indicates that MOF metal-linker bonds exist in dynamic equilibria[28–31] akin to those documented for metal-carboxylate and metal-azolate coordination complexes,[32] and that these equilibria are sensitive to the presence of guest molecules,[33] give rise to strongly temperature-dependent $E_{opt}$ for MOFs in general,[34] and that dynamic metal-linker bonds serve as the "soft-mode" vibrations[35,36] that drive the microscopic mechanism of phase changes in MOFs.[28] This behavior also helps explain the ability of MOFs to undergo post-synthetic cation exchange[37–42] and catalyze reactions at coordinatively saturated metal centers.[43,44] Recent studies of MOF nanoparticles (nanoMOFs) suggests that this behavior becomes size dependent.[24] For instance, the magnetic spin-crossover temperatures of $Fe(TA)_2$ decrease by ~80 K upon size reduction from 160 nm to 6 nm. Similarly, the $E_{opt}$ of $Ti_8O_8(OH)_4$(terephthalate)$_6$ (MIL-125) become more temperature-dependent when reducing particles sizes from 420 nm to 80 nm.[34] In fact, Huang-Rhys parameters ($S$)[45–47]—a dimensionless metric describing the degree of nuclear rearrangement associated with electronic excitation—increase by an order of magnitude from ~8 to 80 with size reduction. Given the widespread importance of metal-ligand bonding to various chemical properties, we expect that enhanced lability and structural flexibility would result in size-dependent behavior across diverse MOF behavior. Here, we describe a combined experimental-computational investigation into the size-dependent $E_{opt}$ of $Fe(TA)_2$ and its family of structural analogs.

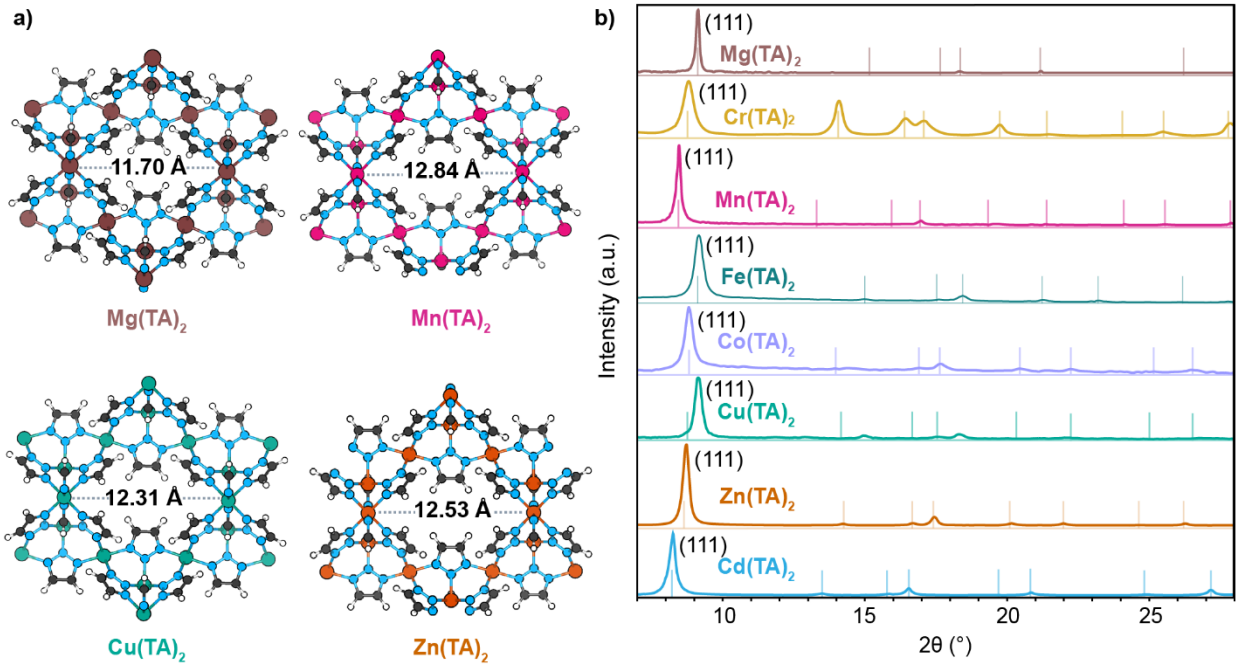


**Figure 1 Synthesis of nanoscale $M(TA)_2$ metal-organic frameworks. (a)** Schematic representation of the secondary building unit (SBU) for each material with metal-metal distances highlighted. **(b)** Powder X-ray diffraction patterns of as-synthesized $M(TA)_2$ nanoparticles collected using Cu Kα radiation (λ = 0.15406 nm). Tick marks below each trace indicate the expected Bragg reflections positions based on reported crystal data.

**Results and Discussion**

To explore the generality of this size-dependent optical behavior, we developed synthetic routes to a family of materials encompassing $M(TA)_2$, $M$ = Mg, Cr, Mn, Fe, Co, Cu, Zn, Cd. **Figure 1a** highlights the range in pore sizes displayed by this otherwise isostructural MOF series. Recently, we demonstrated that differences in pore sizes between $Fe(TA)_2$ and $Cr(TA)_2$ nanoparticle-functionalized electrodes caused redox intercalation potentials to shift by nearly 1 V.[48,49] Although all materials were reported previously as bulk powder or single crystals,[50,51] the nanoscale syntheses required optimization of concentration, temperature, time, metal salt precursor, stoichiometry, and "modulator" additives to achieve reproducible procedures that yield a range of particle sizes. Based on the "seesaw " model of MOF growth developed[52] and demonstrated[15,53,54] by us previously, the overarching strategy was to create reaction conditions that favored off-stoichiometric ratios of metal ions and linkers in solution to deplete MOF growth of reagents and thereby yield nanoparticles. For $Fe(TA)_2$, employing 1-methylimidazole (1-mIm) as a modulator furnished particle sizes between 5-180 nm, as reported previously. [15] Similarly, $Cr(TA)_2$, $Mn(TA)_2$, $Co(TA)_2$, and $Cd(TA)_2$ nanoparticles were synthesized using optimized 1-mIm equivalents detailed procedures are in method section of SI. For the $Mg(TA)_2$ nanoparticle synthesis, however, 1-mIm proved ineffective at modulating particle sizes. Instead, the stronger Lewis base *n*-butylamine (0.5-0.75 mmol) reproducibly generated sizes between 26 - 200 nm (**Fig S1-S15**). Although the precise role of modulators in nanoMOF synthesis as both ligands and acids or bases remains unknown, it is notable that the molar quantity of 1-mIm equals roughly the approximate number surface Fe sites in each $Fe(TA)_2$ synthesis, yet without evidence of 1-mIm incorporation by NMR[15] or thermogravimetric analysis (**Fig. S16**). In certain cases, parameters other than modulator were most effective at controlling particle sizes. The $Cu(TA)_2$ syntheses relied on the triazole:copper stoichiometry (1.5:1 to 3:1), with excess ligand favoring smaller particles. The synthesis of $Zn(TA)_2$, on the other hand, required no modulator, with size control achieved solely by metal:ligand stoichiometry and the metal source selection. Specifically, ZnO produced smaller, well-defined nanoparticles compared to $Zn(NO_3)_2$. Metal ion precursor has been used previously to control MOF particle sizes.[55–57] Here, we propose that the poor solubility creates a sustained, low concentration of $Zn^{2+}$ ions that favors excess ligand-to-metal ratios and arrested particle growth, in contrast to the highly soluble $Zn(NO_3)_2$ salt. In addition to these parameters, nanoscale $M(TA)_2$ nanocrystals were synthesized under more dilute conditions than the bulk syntheses. For example, compared to the reported bulk $Mn(TA)_2$ synthesis, which uses 1 mmol of $Mn(NO_3)_2{\cdot}4H_2O$ and 2.5 mmol 1H-1,2,3-triazole in 10 mL of DEF (0.1 mmol/ml and 0.25 mmol/ml, respectively), the nanoscale synthesis requires 0.3 mmol $Mn(NO_3)_2{\cdot}4H_2O$ and 0.9 mmol of triazole in 10 mL of DMF (0.03 mmol/mL and 0.09 mmol/mL, respectively). The powder X-ray diffraction (PXRD) patterns shown in **Fig. 1(b)** demonstrate the successful synthesis of highly crystalline $M(TA)_2$ nanocrystals. The products are phase-pure, as indicated by the expected reflections presented as tick marks below each trace. However, it is noteworthy that the $Cu(TA)_2$ peaks appear shifted compared to the expected crystal structure Bragg reflections as presented in **Fig. 1(b) and S9**, while the $Cu(TA)_2$ XRD pattern shows peak positions slightly shifted from the simulated pattern, Rietveld refinement analysis confirms good agreement with the expected crystal structure (Figure S9(b)). The observed peak shift can be attributed to the unit cell parameter variations between the nanocrystalline material and the reported bulk material. Furthermore, materials prepared with greater modulator equivalents exhibit broader diffraction peaks, consistent with the formation of nanocrystals. According to the Scherrer equation, the width of diffraction peaks is inversely proportional to crystallite size; as the crystal domains become smaller, peak broadening increases due to limited coherence length within the crystal lattice (for additional PXRD patterns see Figures **S1-S8)**. Scherrer analysis of these patterns provides an estimate of the coherently scattering domain sizes, with average diameters reproducibly spanning 5 nm to >80 nm across the metal series.

To assess the effective size of the prepared nanoparticles were characterized by complementary techniques, including scanning electron microscopy (SEM), dynamic light scattering (DLS), and Scherrer analysis. For all materials, a wide range of particle sizes could be prepared, with all Scherrer, SEM, and DLS characterization included in the Supporting Information (**Fig. S17h**). As proof of the size control of the synthetic routes and to compare optical behavior of similarly sized particles, $M(TA)_2$ materials were prepared with similar sizes in the range of 20-40 nm. **Figure S17 (a-h)** shows SEM images with particle size distribution histograms as insets for each sample. These data reveal quasi-spherical particles roughly twice the corresponding Scherrer size with dispersity indices (Đ) between 0.01 – 0.05, but with most samples showing Đ ~ 0.01. This excellent monodispersity depends on stirring the reaction mixtures, whereas no stirring leads to Đ ~ 0.08. To improve the polydispersity index, it is crucial to fully dissolve the precursor and add the modulator before the linker, as the sequence of addition significantly affects the polydispersity index. DLS corroborates this size dispersity yet reveals hydrodynamic diameters that consistently exceed 5-6 times the particle sizes determined by SEM, suggesting large solvation shells surround the particle surfaces. We used cryo-EM to image small particles of $Co(TA)_2$ (**Fig. S4**), as this technique minimizes radiation damage and preserves the intrinsic structure in solution without need for evacuation.[58,59] Traditional electron microscopy

techniques often induce rapid amorphization and degradation in beam sensitive materials due to high electron dosage, therefore limiting the resolution attainable for small particles. Leveraging cryo-EM, we successfully imaged $Co(TA)_2$ particles with sizes as small as ~4 nm—the smallest nanoMOFs imaged by EM techniques to-date. Simultaneous measurement of zeta potential provides insight into surface charge characteristics. Values ranged from -22 to +102 mV depending on the metal identity, indicating a range of surface compositions and electrostatic interactions. As observed by us with other nanoMOF systems,[53,60,61] all particles exhibit colloidal stability in the absence of deliberate surface-capping ligands. While nanoMOFs and other porous nanocrystal surfaces can be capped deliberately with ligands,[62–65] sum-frequency scattering spectroscopy measurements sensitive specifically to the nanoparticle surfaces,[66] suggest colloidal stability arises from a mixture of self-assembled solvation shells and energetically favorable interactions between linker and solvent molecules.

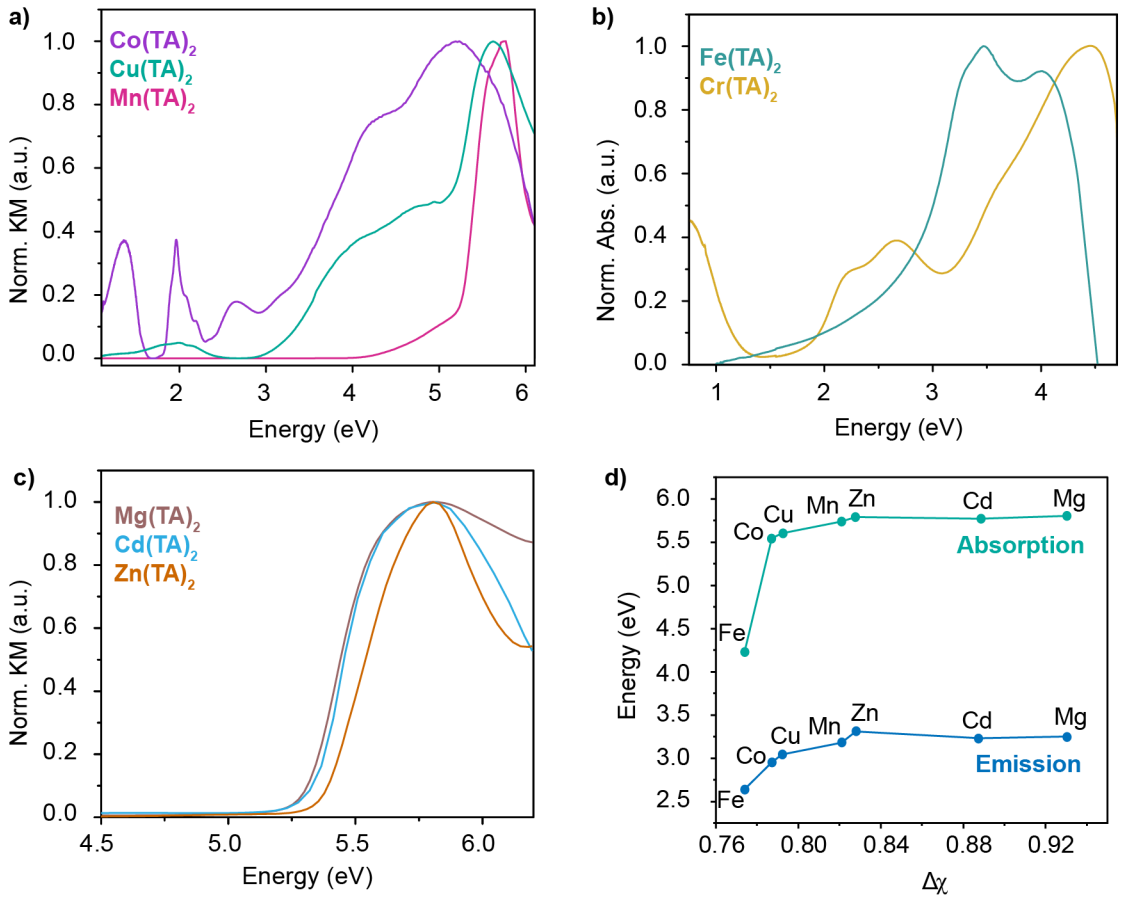


**Figure 2 Optical absorption data of $M(TA)_2$ nanoparticles**. The normalized Kubelka-Munk (KM) function plotted against photon energy (eV) for 20-30nm $M(TA)_2$ nanoparticles. **(a)** open metal d-block ($Cu(TA)_2$, $Co(TA)_2$, $Mn(TA)_2$ **(b)** open metal d-block (solution state UV-Vis) for $Fe(TA)_2$, $Cr(TA)_2$ **(c)** closed shell ($Zn(TA)_2$, $Cd(TA)_2$, and $Mg(TA)_2$.**(d)** charge-transfer energy for absorption and emission maxima plotted against theoretical electronegativity differences for each $M(TA)_2$.

With the ability to control $M(TA)_2$ sample diameters reproducibly, particles of roughly 20-30 nm were prepared to compare the impact of metal identity on optical behavior. **Figure 2** shows the electronic absorption spectra in the UV-visible-near infrared region for a single particle size of each material. Due to the strong light absorption by solvent and light scattering by the colloidal particles, the spectra were collected in diffuse reflectance geometry on dried powders. Solution-state spectra could also be measured for the Cr and Fe variants, which showed clearly resolved absorption bands. For comparison, solution-state and diffuse reflectance electronic absorption spectra of both the Cr and Fe materials are included in the Supporting Information (**Fig 2b, S30**). The solution and solid-state data are in good agreement. In the case of $Fe(TA)_2$, absorption peak positions appear at 3.54 eV, 3.48 eV and 3.45 eV for 16 nm, 84 nm and 130 nm particles respectively. Similarly, the d-d transitions in the $Cr(TA)_2$

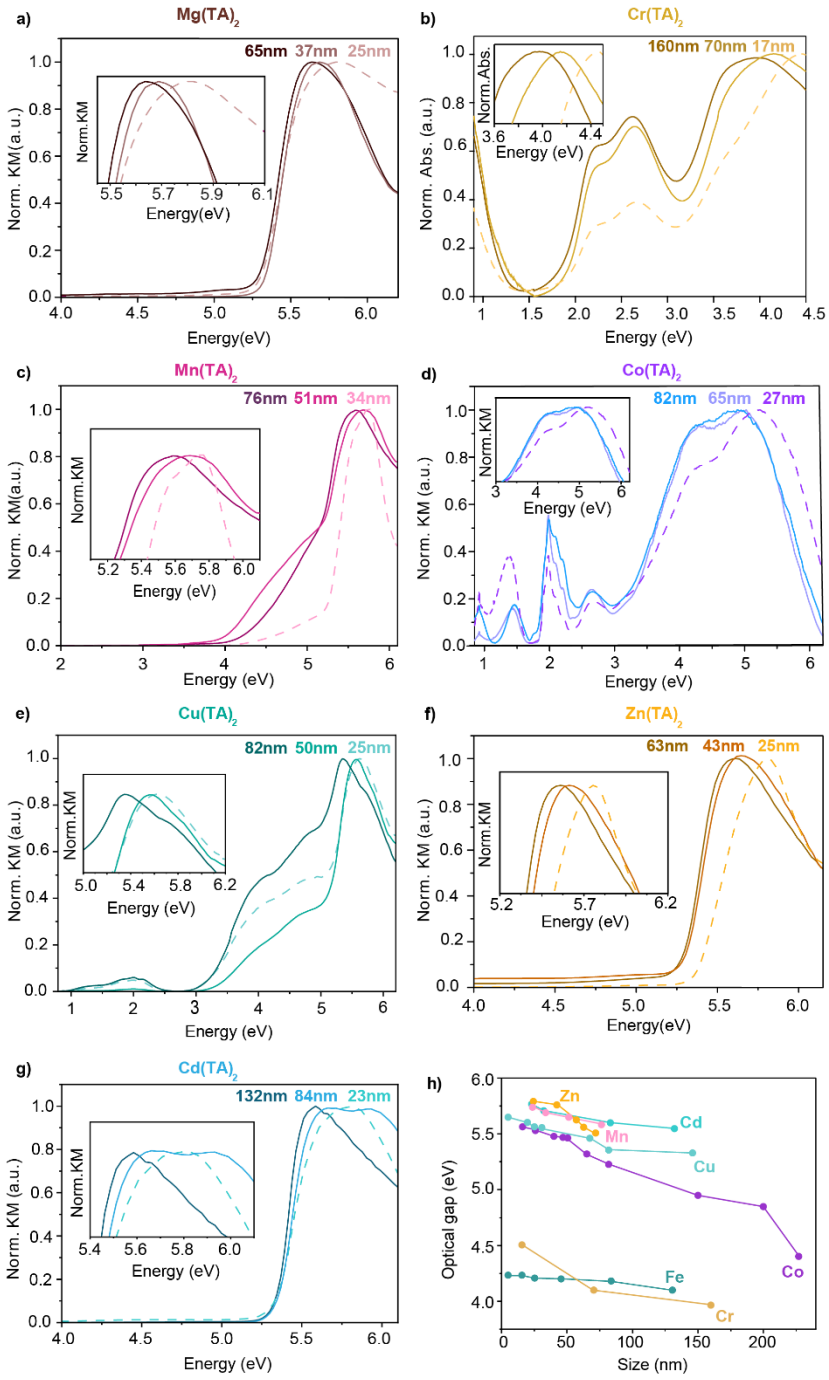


**Figure 3 Size-dependent optical properties of $M(TA)_2$ nanoparticles. (a-g)** Normalized diffuse reflectance and absorption UV-Vis spectra of all $M(TA)_2$ nanoparticles of varying sizes. Spectra are presented as a normalized Kubelka-Munk function or normalized absorption. The inset shows the normalized intensities of the maximum absorption peak position of metal to ligand charge transfer as a function of particle size. **(h)** Optical gap as a function of particle size. For clarity, $Mg(TA)_2$ values are omitted, the optical gap for the 25-nm, 37-nm, and 65-nm particle sizes are 5.74 eV, 5.65 eV and 5.63 eV, respectively.

appear consistently at 2.65 and 2.23 eV in both solution- and solid-state spectra. **Figure 2a and 2b** plot the spectra for the open-shell Cr, Mn, Fe, Co, and Cu ~30 nm nanoparticles in the 0.62 eV - 6.2 eV region, while **Fig. 3c** shows the corresponding spectra for the closed-shell Mg, Zn, and Cd materials. All spectra reveal strong absorption features in the UV range between 3-6 eV. Whereas the closed-shell materials absorb only in this region, the open-shell variants display additional features throughout the visible and infrared. Based on this comparison, we assign the UV features to metal-to-ligand and ligand-to-metal charge transfer (MLCT and LMCT)

events, and the lower-energy features to d-d transitions. The data therefore reveal key electronic differences arising from the coordination environments and other ligand field effects of the $M(TA)_2$ nanoparticle family. In 28-nm $Cu(TA)_2$, the CT band appears at 5.61 eV, with multiple d-d transitions between 1.00–2.40 eV. Although perfectly octahedral $Cu^{2+}$ possesses just a single allowed d-d transition, a lowering of symmetry, such as compression or elongation to the octahedron, produces three allowed d-d transitions that likely to contribute to these peaks. The spectrum of $Co(TA)_2$ shows a CT band around 5.46 eV and multiple d-d transitions between 1–3 eV. Although six-coordinate $Co^{2+}$ is expected for bulk $Co(TA)_2$, the bands between 1–3 eV resemble a convolution of both octahedral and tetrahedral $Co^{2+}$ in a nitrogen ligand field.[67] We propose that these additional features arise from low-coordinate $Co^{2+}$ centers at the exterior surface of the particles, which remain the focus of ongoing investigations. As expected for $Mn^{2+}$, the spectrum of 26-nm $Mn(TA)_2$ lacks any spin-allowed d-d transitions. **Figure 2b** plots the solution-state spectra for the Fe and Cr variants. As reported previously, 24-nm $Fe(TA)_2$ show CT bands at 3.53 eV, and 4.21 eV.[15,68] By handling the particles air-free, the spectrum lacks the intervalence charge transfer (IVCT) band in the infrared expected for $Fe^{2+}$-$Fe^{3+}$ mixed valency. On the other hand, 17-nm $Cr(TA)_2$ shows prominent a IVCT at 0.89 eV, consistent with reports on the bulk material that Cr(TA). arrives with $Cr^{2+}$-$Cr^{3+}$ mixed valency even when prepared air free.[69] As a result, the spectrum shows several broad d-d transitions between 2 and 3 eV expected for octahedral $Cr^{3+}$ as well as CT bands around 4.5 eV. All open-shell variants display a multitude of transitions between 3-5 eV less intense than the high-energy features, which we ascribe to various LMCT transitions.

Assigning optical gaps to MOFs poses significant challenges due to the typically localized nature of their orbitals.[8] Even in semiconductors such as $Fe(TA)_2$ and $Cr(TA)_2$, the various ligand field transitions complicate assignment of $E_{opt}$. Therefore, to compare optical behavior between the $M(TA)_2$ family and understand the impact of the metal ion identity, we analyzed the highest-energy CT bands that appear in all materials. As originally described by Jørgensen, [70] CT transitions may also be termed "redox transitions" because they are closely related to the redox properties of the donor and acceptor orbitals involved in the electronic excitation. As a result, CT energies should generally increase as the difference in electronegativity ($\Delta\chi$) between the donor and acceptor orbitals increases. **Figure 2d** plots the highest-energy CT band peak energies versus computed electronegativity differences between the corresponding metal cations and the nitrogen anion.[71] The monotonic increase in CT peak energies with $\Delta\chi$ strongly supports the assignment of these bands to CT transitions and illustrates that the optical behavior of these materials is more than the simple combination of the constituent parts. The solution-state photoluminescence (PL) spectra of all ~ 30 nm $M(TA)_2$ in 5-mM DMF further highlights the importance of metal-linker interactions to the optical behavior, as shown in **Fig. S18**. Additional spectra of the absorption and PL profiles overlayed for each metal variant are included in **Fig. S19.** With the exception of the Cr variant, which does not fluoresce, and the Fe PL spectrum, the PL of all materials resemble the solution-state fluorescence of 1,2,3-triazoale in DMF, with a few notable exceptions: 1) the PL peak maxima depend on the metal identity and follow the same trend with $\Delta\chi$ as the absorption profiles, 2) the signal-to-noise is greatly improved, and 3) the PL profiles show well-resolved vibronic structure. Rather than a >3 eV Stokes shift, we interpret these PL profiles as arising from a combination of direct excitation of the linker followed by linker-based emission and excitation across the $E_{opt}$, followed by efficient energy transfer to the linker-based excited state akin to trap-based fluorescence. The excitation wavelength of 200 nm is sufficient for both forms of excitation. Nevertheless, the PL peak positions shifting by 110 meV with metal identity indicate significant interactions between the metal and linker orbitals. We attribute the greater signal-to-noise to the matrix isolation of the linkers in relatively rigid geometries. Rather than tumbling freely in solution as isolated molecules, the triazolate species exhibit improved PL intensity because the orbitals are held rigidly in place at angles less ideal for self-quenching. We attribute the lack of Cr emission and the unique PL profile of the Fe variant to the redox activity of the metal centers, which could act as hole or electron traps. Therefore, we tentatively assign to the Fe PL spectrum to trap-based emission involving hole migration to a $Fe^{2+}$ center followed by recombination with electrons in the CT excited state. Few if any reports have demonstrated similar trap-based emission in MOF materials.[72–74]

All $M(TA)_2$ materials show size-dependent optical absorption and photoluminescence behavior. **Figure 3** includes representative absorption spectra for three sizes of each material with insets that highlight the size dependence of the highest-energy CT bands. The spectra consistently reveal that these UV absorption features blue-shift from the reported bulk values as the particle sizes decrease, regardless of whether they possess open-shell or closed-shell electron configurations. For $Mg(TA)_2$ the absorption maximum shifts from 5.80 eV (25 nm) to 5.68 eV (37 nm) and 5.63 eV (65nm), while for $Cr(TA)_2$ it shifts from 4.5 eV (17nm) to 4.1 eV (70 nm) and 3.9 eV (160 nm). The CT band of $Mn(TA)_2$ similarly redshifts from 5.74 eV (34 nm) to 5.60 eV (76 nm) and for $Co(TA)_2$ it redshifts from 5.46 eV (27 nm) to 5.23 eV (84 nm). $Cu(TA)_2$ exhibits an MLCT band that shifts from 5.61 eV for 25 nm to 5.40 eV for the largest particle sizes (84 nm). **Fig. 3(f, g)** shows that the $Zn(TA)_2$ and $Cd(TA)_2$ follow a similar trend of optical shift with the change in size. In Zn the optical gap shifts from 5.68 eV to 5.87 eV by increasing from 25 nm to 63 nm and in $Cd(TA)_2$ the optical gap shifts from 5.55 eV to 5.57 eV

by increasing from 23 nm to 132 nm. **Figure 3h** collates the CT energies for all $M(TA)_2$ nanoMOFs for a larger sample collection of sizes. Given the qualitative similarity between these trends and that they arise for a wide range of open- and closed-shell metal ions, these data strongly suggest a general size-dependence to the optical absorption that persists for particle sizes well beyond the typical regime for quantum confinement. The effect on the optical behavior is weaker, however, with a universal slope of roughly ~ 4.5 meV per nanometer whereas quantum confinement leads to blueshifts of > 1 eV per nanometer change in diameter. In addition to electronic absorption, size reduction also impacts PL spectra for all materials. **Figure 4** includes a few representative materials with the complete set of spectra that shows size dependent PL and absorption. Whether open-shell $Co(TA)_2$ or closed-shell $Cd(TA)_2$ or $Mg(TA)_2$, the PL spectra, even though predominantly triazolate in character, blue-shift in the smaller nanoparticles. Interestingly, the slope in PL emission energy versus size mirror the slope from absorption spectra (**Fig. 2d**). These results indicate that size reduction involves a mechanism that influences even the localized orbitals of the linker as well as the more diffuse MLCT donor-acceptor orbitals. In order of increasing slope, we observe for the various $M(TA)_2$ materials: Fe (1meV/nm), Cd (1.92 meV/nm), Cu (2.34 meV/nm), Mn (2.79 meV/nm), Cr (3.47 meV/nm), Co (4.92 meV/nm), and Zn (6.47 meV/nm). Tentatively, we propose that this ordering arises from the strength and lability of the metal ligands bonds. Whereas the low-spin ferrous centers resist bond elongation, the zero crystal field stabilization energy of the zinc analog accommodates significant bond distortions.

The size-dependent optical behavior of $M(TA)_2$ nanoparticles challenges conventional models based on quantum confinement or electrostatic interactions. Colloidal nanocrystals that exhibit quantum confinement typically possess binary semiconductor lattices such as CdSe or InAs with band-type charge transport. Quantum confinement arises from semiconductors being prepared as particles with diameters smaller than their characteristic Bohr excitonic diameter. Confining photogenerated electron-hole pairs to such constricted volumes causes the mobile charges to behave as particles in a finite well potential. As a result, electronic absorption occurs at discrete energies that become progressively blue-shifted as particle sizes decrease, according to the relationship $E_{opt} \propto 1/R^2$, R = radius. Ever-improving synthetic methods have enabled diverse semiconductor compositions, narrow particle dispersity, and numerous applications in fields such as bioimaging, light-emitting diodes (LEDs), and photovoltaics.[75–77] The data in **Fig. S20** show that CT band energies of $M(TA)_2$ nanoparticles defy a $1/R^2$ relation from quantum confinement or a 1/R relation from electrostatic interactions. This finding was first reported for $Fe(TA)_2$ particles,[15] but was suspected to arise from features specific to the Fe variant. Furthermore, only the Fe and Cr variants exhibit

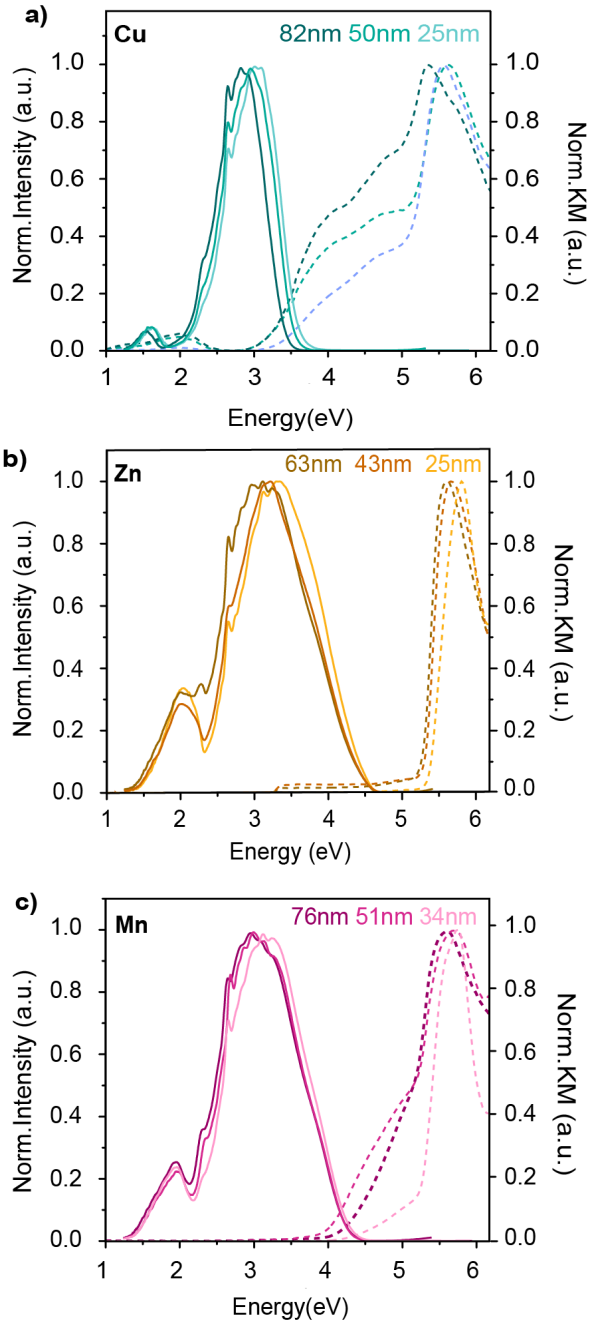


**Figure 4 Size-dependent photoluminescence and electronic absorption spectra of $M(TA)_2$ for three different particle sizes**. a) $Cu(TA)_2$ b) $Zn(TA)_2$ and c) for $Mn(TA)_2$. Solid lines represent PL spectra and dashed lines represent absorption spectra.

semiconductor behavior, making it unlikely that all materials could display quantum confinement for particles larger than a few nanometers. Instead, the CT energies for all $M(TA)_2$ nanoparticles linearly increase as particle sizes decrease. As shown in **Fig. S20**, plotting the CT energies against $1/R^2$ or 1/R produces non-linear trends, further arguing against quantum confinement. These plots suggest, however, that the mechanism of size-

dependent optical behavior alters depending on the particle size. A clear change in slope appears in these plots at diameters corresponding to roughly 20 nm, which was reported previously for $Fe(TA)_2$. In other words, the mechanism of size dependent optical behavior may scale linearly with $1/R^2$ or $1/R$ but that the scaling relation changes drastically as surface-to-volume ratios become large. Quantum confinement and other optical changes due to electrostatic interactions are also typically relevant only to length scales below 20 nm.

Surface chemistry was explored as a potential origin of size-dependent optical shifts because mid-gap orbitals and other surface-related effects would persist for particles as large as 200 nm. First, size-dependent oxidation was considered since the surface sites of smaller particles are expected to become more reactive. As shown previously for $Fe(TA)_2$, however, the percentage of $Fe^{3+}$ observed by Mössbauer was independent of particle size.[15] Experiments were meticulously conducted under inert conditions to minimize oxidation, which resulted in the lack of an IVCT band for $Fe(TA)_2$ and $Co(TA)_2$, as shown in **Fig. 2 and 3**. Although $Cr(TA)_2$ exhibits an expected IVCT band in **Fig. 3(b)**, which indicates the presence of $Cr^{3+}$, the shift in MLCT was independent of IVCT intensity or position across all sample sizes. Importantly, the generality of this effect to redox-inactive materials such as the Mg, Zn and Cd variants further refutes metal oxidation as the origin of size-dependent optical behavior. Inspired by reports on the effect of surface dipoles causing $E_{opt}$ shifts in colloidal quantum dots,[78–80] we examined whether solvent, as a dielectric, could modulate the electrostatic effect of potential surface charges and the resulting shift to MLCT bands. Solution-state absorption spectra were collected on 48-nm particles suspended in dimethyl formamide, methanol, propylene carbonate, and benzonitrile **(Fig. S21, Table S3)**. These solvents were chosen due to differences in their Gutmann donor numbers.[81] We expected solvent molecules to stabilize the electronic ground state through coordinative binding to charged species at the surface or by acting as a dielectric to stabilize the charge-separated electronic excited state. The effect of solvent on the absorption spectra was minimal, however. Furthermore, the spectra in **Fig. 2** and **3** corresponds to solid-state measurements performed on fully activated, solvent-free samples. In other words, these measurements consistently reproduced size-dependent optical shifts far larger than the minor effect of introducing solvent. Whatever the correct mechanism, it must operate across tens of hundreds of nanometer length scales, unlike quantum confinement.

Because optical behavior arises from metal- and linker-based orbitals, we propose that the size-dependent optical shifts result from size-dependent metal-linker bonding. Recent evidence suggests that the size-dependent spin crossover behavior of $Fe(TA)_2$ nanoparticles originates from iron-triazolate bonding becoming more dynamic as particle sizes decrease. This enhanced flexibility allows the metal-linker bonds to adopt a wide range of conformations similar in energy rather than the bonds simply becoming longer or shorter. Crystallographically, this effect should manifest in a change to unit cell parameters or as microstrain, which describes a distribution of bonding parameters about an average expected crystallographic value. Recent evidence from our lab using variable-temperature PXRD data suggests that indeed various crystallographic parameters vary strongly with nanoMOF size and that smaller particles display greater thermal displacement parameters and thermal expansion coefficients. Importantly, these size-dependent crystallographic parameters also manifested in microstrain that increased for smaller particles.[82] Elastic strain fields in nanocrystals are known to propagate coherently across entire particles up to 30-50 nm, and in some cases even approach ~100-200 nm, without requiring inelastic relaxation. For instance, Li Et al. showed that

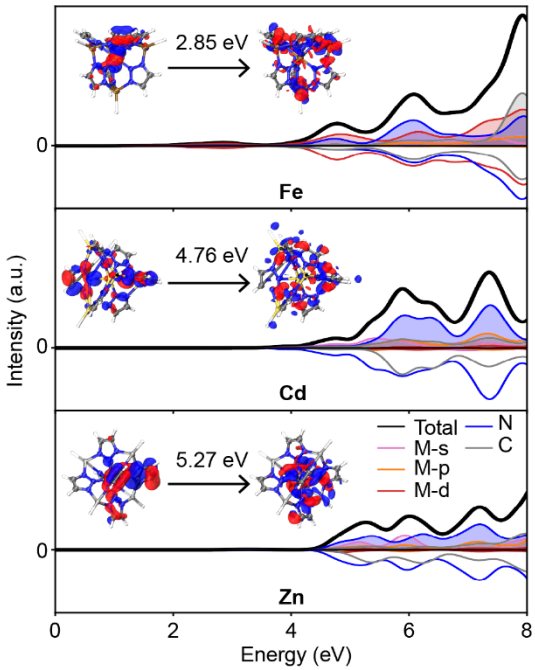


**Figure 5 The linear response time-dependent density functional theory UV-Vis absorption plot for the non-perturbed Kuratowski clusters for Fe, Cd and Zn** (A-C). In each plot the absorption spectrum is plotted as a black trace, in color is the molecular orbital (MO) decomposed absorption spectrum. Positive MO values correspond to the arriving orbitals, while negative values indicate the character of the leaving orbitals. Inset into each plot is leaving/hole (left) and arriving/electron (right) natural transition orbitals responsible for each absorption feature.

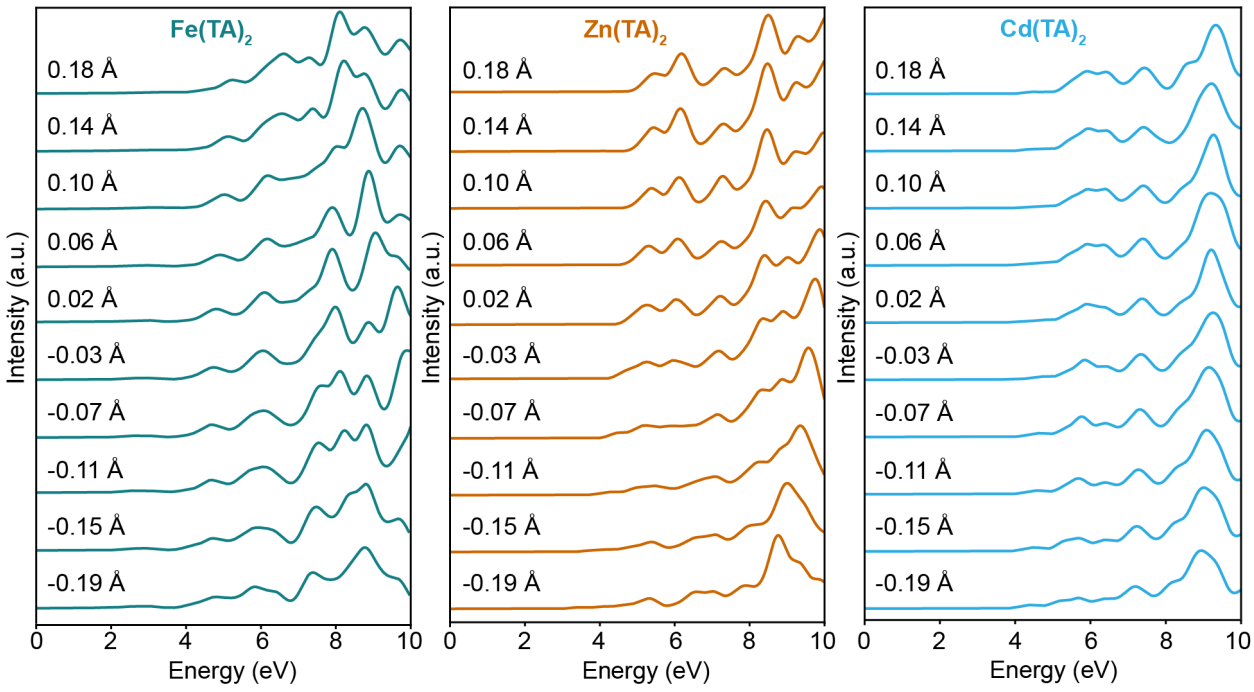


**Figure 6 Simulations of lattice strain.** Linear-response time-dependent density functional theory (TD-DFT) absorption spectra for $Fe(TA)_2$, $Zn(TA)_2$, and $Cd(TA)_2$ Kuratowski-type clusters. Spectra are calculated for clusters with metal-pseudo-hydrogen bond lengths modified from the geometry determined without constraints.

nanostructures can support elastic distortions up to ~10% over tens of nanometer length scales that directly impact optical and electronic behaviors.[83]A few isolated reports have documented size-dependent microstrain in nanoparticles as well.[84–86]

Ample literature evidence would support size-dependent microstrain as the origin of the size-dependent optical behavior of $M(TA)_2$ nanoparticles. In 1950, Schockley and Bardeen introduced the fundamental concept of band gap modulation via lattice expansion or contraction.[87] Recently, lattice strain—either through external stimuli or lattice mismatch in heterostructures—has attracted widespread interest for tuning optical behavior. For instance, applying compressive strain to the inorganic cubic halide perovskite $Sr_3PBr_3$ reduces the band gap from 1.528 eV to 1.23 eV at −4% strain, while tensile strain increased it to 1.723 eV at +4% strain.[88] Similarly, density functional theory (DFT) studies have demonstrated that germanium, a prototypical indirect band gap material, can be transformed into a direct band gap semiconductor via uniaxial strain applied along the [111] crystallographic direction.[89] Lattice mismatch in (Al/Ga)N-core shell heterostructures causes an optical blue-shift from 3.40 to 3.64 eV in the GaN layer. Strain engineering has also been used to modulate the electronic and optical properties of 2D materials, particularly transition metal dichalcogenides such as $MoS_2$, $WS_2$ and $WSe_2$.[90–92] In these systems, both uniaxial and biaxial tensile strain leads to redshifts in the optical absorption and photoluminescence peaks due to band gap narrowing.[93] For instance, tensile strain in monolayer $MoS_2$ induces the direct band gap red shift approximately 70 meV per 1% strain.[94] Conley et al. showed that the band gap of monolayer $WSe_2$ decreases linearly under applied strain. These optical shifts were attributed to the changes in orbital overlap and symmetry breaking at the band edges, particularly between the transition metal d-orbitals and chalcogen p-orbitals. The structural flexibility of MOFs is illustrated in their ability to accommodate epitaxial, uniaxial, hydrostatic, and thermally induced strain.[95–98] This adaptability has opened new opportunities in strain engineering, especially for emerging applications in sensing and catalysis.[99] The tunability of MOFs under mechanical stress has been further demonstrated through theoretical simulations. In one study, DFT-based lattice modification of UiO-66 (Zr and Ce) from −3% (compressive) to +3% (tensile) strain led to systematic tuning of the band gap, ranging from 2.50 eV under compressive strain to 1.45 eV under tensile conditions, and band gap of 2.09 eV at −3% strain.[100] In another case, defect engineering in zirconium-based MOFs was shown to induce internal strain, facilitating controlled structural distortions and resulting in band gap modulation.[101]

To investigate the possibility of size-dependent metal-linker bonding as the origin of the optical shifts, time-dependent density functional theory calculations were performed on the so-called "Kuratowski clusters"[102] as discrete molecular models of $M(TA)_2$. Numerous computational studies employ this family of clusters to model the catalytic, cation exchange, and other behavior of $Zn_5Cl_4$(bis(1,2,3-triazolato[4,5-b][4',5'-

i])dibenzodioxin)$_3$ (MFU-4*l*) and related MOFs.[103,104] For a representative cross section of the different electronic structures, Fe(TA)$_2$, Zn(TA)$_2$, and Cd(TA)$_2$ were targeted for this study due to their closed- and open-shell nature. This optimization resulted in M(TA)$_2$ clusters with average M-H bonds of (2.26 Å, 2.17 Å, and 1.89 Å) for Fe, Cd, and Zn(TA)$_2$ and average M-N distances of (1.94 Å, 2.35 Å, and 2.06 Å) for Fe, Cd, and Zn(TA)$_2$. Calculations were performed using the Stuttgart/Dresden pseudopotentials and associated basis at a B3LYP level of theory in the Gaussian software package.[105–109] **Fig. 5** shows the simulated spectra for Fe, Cd, and Zn(TA)$_2$ with insets representing natural transition orbitals responsible for each transition feature. Inspection of the molecular orbitals supports the assignment of transitions above 3 eV to involved various MLCT and LMCT bands, whereas transitions below involve predominantly d-d transitions.

Given the good agreement between the simulated and experimental spectra, the effect of microstrain was studied in terms of differing metal-ligand covalency and bond length. By altering the distance between the metal centers and the TA ligands, the effects of compression and expansion could be modeled. **Figure 6** shows that relatively small perturbations of 0.01 Å manifest in large shifts to peak positions and overall spectral shape. Analysis of the leaving and arriving orbitals involved in these transitions show similar character as the metal-triazolate bond length is adjusted, indicating that these spectral shifts are caused by the changing electronic environment of the metal centers (**Fig. 5**). There are two effects at play: the changing polarization of the metal and TA linkers, and the composition of the band edges. As the distance between the metal and TA linker shrinks, the band gap decreases. This decrease in band gap causes the optical features to red-shift, as observable in the PDOS plots (**Fig. S22**). This band shrinking arises from the partial effective oxidation of the metal and reduction of the ligands causing the molecular orbitals (MOs) to shift. As the metal TA distance increases the band gaps widen. However, in the absorption plots they appear to redshift. This seeming contradiction arises because as the bands open the number of orbitals on the edges increase. This orbital density increase leads to more responses near the band gap, giving rise to the observed red shifting. Since these changes to the absorption bands arise from the changing electronic environment of the metal and TA centers, similar responses can be observed when the charge of the pseudo-hydrogen is adjusted, which is provided in the SI (**Fig. S23**). These simulations help

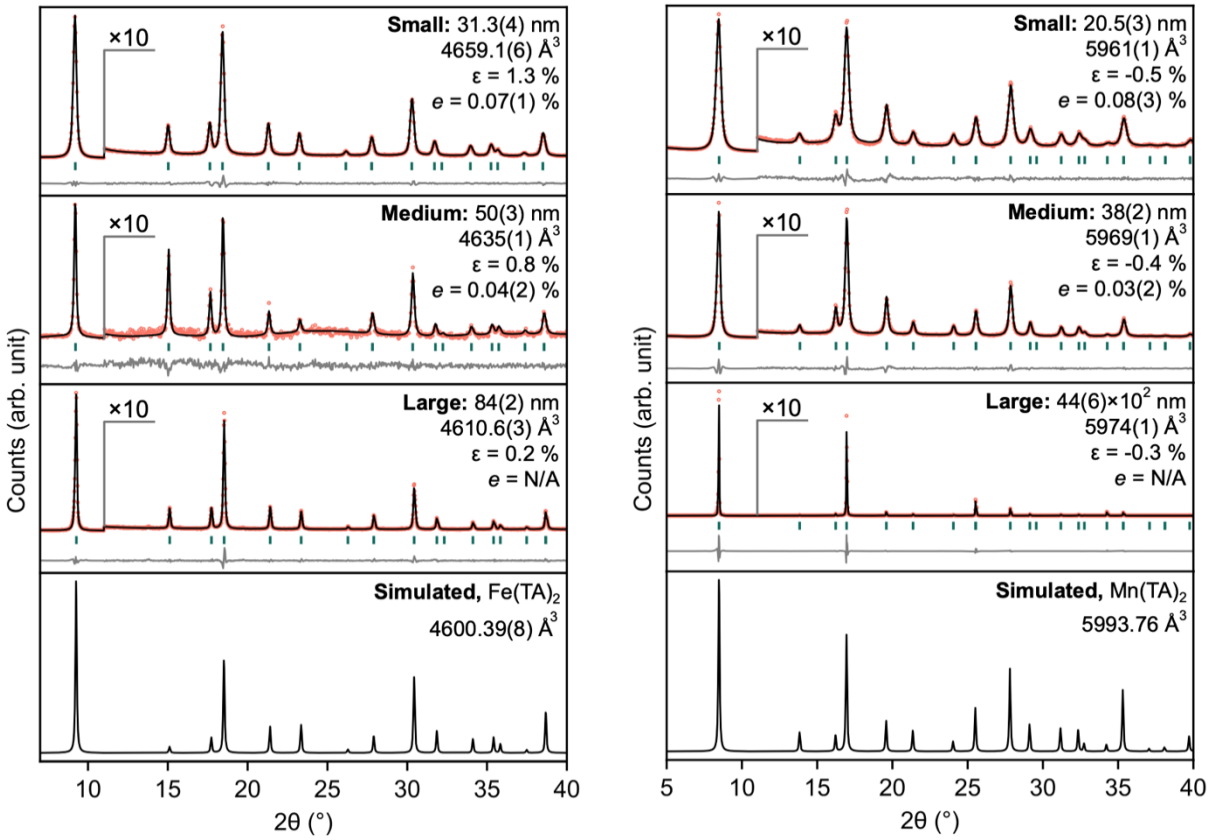


**Figure 7**. Structural refinement and size-dependent strain analysis of Mn(TA)$_2$ and Fe(TA)$_2$ nanoparticles. High-resolution PXRD patterns and obtained Pawley fits, showing experimental (red circles) calculated intensities (black lines), difference curves (gray), and expected peak positions (green tick marks) for three distinct particle size regimes: small, medium, and large. The crystalline domain size (nm), unit cell volume (Å$^3$), strain (ε, %), and microstrain (*e*, %) is given for each sample.

corroborate experimental findings for several classes of materials that microstrain as small as 1% may lead to $E_{opt}$ shifts exceeding 100 meV.

For experimental insight into whether the optical behavior arises from size-dependent metal-ligand bonding, the crystallographic microstrain parameters of $M(TA)_2$ nanoparticles were evaluated. Experimentally, both $Mn(TA)_2$ and $Fe(TA)_2$ exhibit systematic changes in the unit cell parameters with decreasing domain size as presented in **Fig. 7**. Detailed analyses of the experimental patterns reveal an increase in both overall strain (ε) and the upper-limit microstrain (*e*) with decreasing domain sizes, elucidated using double-Voigt integral breadth methods,[110,111] as implemented in TOPAS Academic V6[112] with corrections to any instrument-dependent line broadening. For $Mn(TA)_2$, the unit cell contracts from 5993.76 $Å^3$ (bulk) to 5961 $Å^3$ (20.5 nm), accompanied by strain of up to -0.5% and microstrain of 0.08% with respect to reported bulk material. As shown in **Fig. 3**, the CT band energy increases from 5.6 eV to 5.74 eV in going from the larger (44 nm) to smaller size (20 nm) of $Mn(TA)_2$. In contrast, $Fe(TA)_2$ shows volume expansion from 4600.39 $Å^3$ (bulk) to 4659.1 $Å^3$ (31.3 nm) upon decreasing the size, with a strain of 1.3% and microstrain of 0.07% being observed for the smallest sample, and an optical blue shift in going from the large size to small size $Fe(TA)_2$. In $Cd(TA)_2$, $Cr(TA)_2$ and $Co(TA)_2$ the unit cell volume contracts and $Zn(TA)_2$ show slight volume expansion with increase in microstrain for small size as presented in **Fig. S24-27**. $M(TA)_2$ nanoparticles exhibit optical shifts with 0.5-1.3% strain. For comparison, halide perovskites[113] show 35-60 meV shifts with ~2.4% strain, 2D materials like $MoS_2$ exhibit ~70 meV per 1% strain,[114] and III-V semiconductor heterostructures (GaAs/InP) display up to 260 meV.[115] The blueshift with either compression or expansion is consistent with the foregoing computational results that spectral shifts arise from both metal-linker bond contraction or elongation, and with literature precedent of >100 meV optical shifts with ~1% strain. We recently reported preliminary observations of size-dependent microstrain in $Fe(TA)_2$[116]. The present work significantly extends beyond that initial report by systematically investigating an entire isostructural MOF family, performing rigorous quantitative strain analysis through refinements, employing comprehensive DFT calculations for mechanistic understanding, incorporating excitation-dependent photoluminescence studies, and benchmarking our findings against established material classes. These substantial advancements transform preliminary observations into a comprehensive framework for understanding and rationally tuning optical properties in MOF nanoparticles.

To evaluate whether size-dependent optical shifts extend beyond the $M(TA)_2$ family, we examined structurally diverse MOF systems including the imidazolate-based ZIF-8, the carboxylate-based CuBTC ($Cu_3$(trimesate)$_2$, HKUST-1), as shown in Figure 8 and the heterometallic carboxylate MUV-10(Ca), MIL-125 and UiO-66 and S41. These materials differ substantially in metal coordination (tetrahedral Zn-imidazolate, paddlewheel Cu-carboxylate, multinuclear Ca/Ti-carboxylate clusters) and framework topology. Nevertheless, all three systems exhibit blue-shifted absorption edges with decreasing particle size: ZIF-8 shifts from 5.46 eV (633 nm particles) to 5.64 eV (47 nm), CuBTC from 4.33 eV (80 nm) to 4.73 eV (47 nm), and MUV-10(Ca) from 4.6 eV (71 nm) to 5.0 eV (24 nm).

It is well established that the d-d transition of CuBTC is highly sensitive to its local environment, particularly the presence of coordinated solvent molecules.[117–119] To eliminate the external effects and isolate the intrinsic optical response, we carefully removed the solvent under vacuum prior to measurement, ensuring that any variation in absorption energy arises solely from particle size. Under these controlled conditions, we observe systematic size-dependent shifts in the d-d transition energy consistent with literature

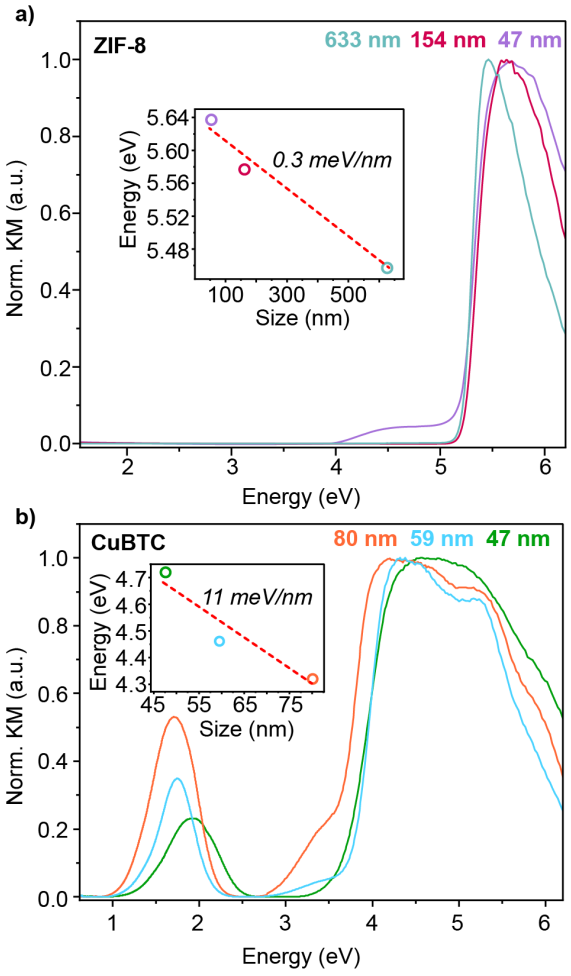


**Figure 8** Size dependent absorption response of a) ZIF-8 b) CuBTC for three different sizes. Inset represents the energy of highest energy transition.

precedent. In bulk CuBTC or large single crystals (10-20 um) the d-d transition appears at approximately 1.47 eV.[117] As particle size decreases to the nanoscale (~50 nm) the transition shifts to ~1.77 eV.[120] In thin-film or highly nanostructured CuBTC system with crystallite domains of 20-100 nm, the d-d absorption edge extends to 2.47 eV, further demonstrating the strong size dependence of Cu(II) electronic states.[118] In our study, CuBTC nanoparticles exhibit this transition at 1.73 eV for 80 nm, 1.75 eV for 59 nm and 1.91 eV for smallest 47 nm particles (Figure S46). The shift magnitude of ~5 meV/nm is consistent with the strain-optical coupling observed across $M(TA)_2$ series (~4.5 meV/nm), demonstrating that this phenomenon extends beyond triazolate frameworks. Extensive previous analysis of so-called copper paddlewheel clusters indicates that this band involves Cu-Cu electronic transitions with strong sensitivity to inter-copper distances. Therefore, the size-dependence of the visible band of CuBTC suggests significant changes to bond distances upon size reduction.[121] By contrast, the slopes of 0.3 meV/nm and 11 meV/nm for the ZIF-8 and CuBTC charge transport bands indicates that this size effect likely depends on the metal-ligand bond lability, where the strong Zn-imidazolate bonds of ZIF-8 lead to a shallow slope and the labile Cu-carboxylate exhibit strong sensitivity.

The strain analysis reveals a clear correlation between particle size and lattice strain. For ZIF-8 (Figure S39), smaller nanocrystals (47 nm) exhibit higher microstrain ($\varepsilon = 0.7\%$) compared to larger particles (633 nm, $\varepsilon = 0.5\%$). This trend is even more pronounced in CuBTC (Figure S40), where the smallest nanocrystals (47 nm) show $\varepsilon = -0.3\%$, which becomes increasingly negative to $\varepsilon = -0.7\%$ for the 80 nm particles, reflecting systematic lattice contraction. Similarly, in MUV-10 (Ca) (Figure S42, the smallest nanocrystals (24 nm) display the highest microstrain ($\varepsilon = 1.2\%$) and significant size broadening ($e = 0.14\%$), while larger particles (200 nm) show reduced strain ($\varepsilon = 1.0\%$). These observations demonstrate that size-dependent strain and optical modulation represent a general phenomenon in MOF nanoparticles. The universality of this effect suggests that rational control of particle size offers a broadly applicable strategy for tuning optical properties across diverse MOF families.

**Conclusion**

This combined experimental-computational investigation provides an explanation for size-dependent optical behavior based in long-range crystallographic strain rather than conventional arguments of quantum confinement. Previous evidence of size-dependent $E_{opt}$ in $Fe(TA)_2$ opened the possibilities of size-dependent metal oxidation, surface-based midgap orbitals, or magnetic interactions as the origin, but this study excludes these explanations by demonstrating the generality of size-dependent optical behavior to a wide range of $M(TA)_2$ materials and several notable examples of MOFs with dissimilar metal-linker compositions. These systematic studies required the synthesis of $M(TA)_2$ with controllable sizes and narrow dispersities. Although conventional nanoMOF syntheses rely on modulator additives, our optimized protocols made use of metal precursor, concentration, and modulator identity. Nevertheless, the effect of these parameters is to minimize metal ion availability in solution, in line with the "Seesaw Model" of nanoMOF growth. Computational simulations employing the Kuratowski cluster suggest that relatively small changes to metal-linker bond covalency and bond length could shift CT band positions so drastically as to alter the qualitative shape of the spectra entirely. Indeed, crystallographic analysis of the $Fe(TA)_2$ and $Mn(TA)_2$ nanoparticles reveal size-dependent microstrain exceeding 1% for the smallest particles. Optical absorption features in other MOFs similarly shift with particle size, suggesting size-dependent bonding operates in them as well. Taken together, these results highlight the importance of delocalized mechanical properties, in addition to electronic interactions, in understanding the size-dependent optical behavior of materials in general.

**ASSOCIATED CONTENT**

**Supporting Information.**

The Supporting Information is available free of charge at http://pubs.acs.org.

Details of syntheses and characterization, computational details, additional spectra.

**AUTHOR INFORMATION**

Corresponding Author

*cbrozek@uoregon.edu

**ACKNOWLEDGMENT**

This material is based upon work supported by the Department of Energy through the Office of Basic Energy Sciences under Grant DE-SC0022147. C.K.B acknowledges the Research Corporation for Science Advancement (Cottrell Award). This work made use of the CAMCOR facility of the Lorry I. Lokey Laboratories at the University of Oregon. X.L. acknowledges support by the University of Washington Molecular Engineering Materials Center (DMR-2308979). This work was facilitated though the use of advanced computational, storage, and networking infrastructure provided by the Hyak supercomputer system at the University of Washington. A portion of this research was supported by NIH grant R24GM154185 and performed at the Pacific Northwest Center for Cryo-EM (PNCC) with assistance from Marcelo De Farias.

**References**

(1) Brus, L. E. A Simple Model for the Ionization Potential, Electron Affinity, and Aqueous Redox Potentials of Small Semiconductor Crystallites. *J. Chem. Phys.* **1983**, *79* (11), 5566–5571. https://doi.org/10.1063/1.445676.

(2) Brus, L. E. Electron–Electron and Electron-hole Interactions in Small Semiconductor Crystallites: The Size Dependence of the Lowest Excited Electronic State. *J. Chem. Phys.* **1984**, *80* (9), 4403–4409. https://doi.org/10.1063/1.447218.
(3) Jin, P.; Li, C. M.; Zhang, Z. Y.; Liu, F. Q.; Chen, Y. H.; Ye, X. L.; Xu, B.; Wang, Z. G. Quantum-Confined Stark Effect and Built-in Dipole Moment in Self-Assembled InAs/GaAs Quantum Dots. *Appl. Phys. Lett.* **2004**, *85* (14), 2791–2793. https://doi.org/10.1063/1.1801678.
(4) Yalcin, S. E.; Labastide, J. A.; Sowle, D. L.; Barnes, M. D. Spectral Properties of Multiply Charged Semiconductor Quantum Dots. *Nano Lett.* **2011**, *11* (10), 4425–4430. https://doi.org/10.1021/nl2026103.
(5) Empedocles, S. A.; Bawendi, M. G. Quantum-Confined Stark Effect in Single cdSe Nanocrystallite Quantum Dots. *Science* **1997**, *278* (5346), 2114–2117. https://doi.org/10.1126/science.278.5346.2114.
(6) Tsui, E. Y.; Hartstein, K. H.; Gamelin, D. R. Selenium Redox Reactivity on Colloidal CdSe Quantum Dot Surfaces. *J. Am. Chem. Soc.* **2016**, *138* (35), 11105–11108. https://doi.org/10.1021/jacs.6b06548.
(7) Schival, K. A.; Gipson, R. R.; Prather, K. V.; Tsui, E. Y. Photoinduced Surface Charging in Iron-Carbonyl-Functionalized Colloidal Semiconductor Nanocrystals. *Nano Lett.* **2019**. https://doi.org/10.1021/acs.nanolett.9b02726.
(8) Fabrizio, K.; Le, K. N.; Andreeva, A. B.; Hendon, C. H.; Brozek, C. K. Determining Optical Band Gaps of MOFs. *ACS Mater. Lett.* **2022**, *4* (3), 457–463. https://doi.org/10.1021/acsmaterialslett.1c00836.
(9) Lin, K.-F.; Cheng, H.-M.; Hsu, H.-C.; Lin, L.-J.; Hsieh, W.-F. Band Gap Variation of Size-Controlled ZnO Quantum Dots Synthesized by Sol–Gel Method. *Chem. Phys. Lett.* **2005**, *409* (4), 208–211. https://doi.org/10.1016/j.cplett.2005.05.027.
(10) Khatun, N.; Rini, E. G.; Shirage, P.; Rajput, P.; Jha, S. N.; Sen, S. Effect of Lattice Distortion on Bandgap Decrement Due to Vanadium Substitution in TiO2 Nanoparticles. *Mater. Sci. Semicond. Process.* **2016**, *50*, 7–13. https://doi.org/10.1016/j.mssp.2016.04.002.
(11) Bredas, J.-L. Mind the Gap! *Mater Horiz* **2014**, *1* (1), 17–19. https://doi.org/10.1039/C3MH00098B.
(12) Narvaez, G. A.; Bester, G.; Zunger, A. Excitons, Biexcitons, and Trions in Self-Assembled (In,Ga)As GaAs Quantum Dots: Recombination Energies, Polarization, and Radiative Lifetimes versus Dot Height. *Phys. Rev. B - Condens. Matter Mater. Phys.* **2005**, *72* (24), 1–10. https://doi.org/10.1103/PhysRevB.72.245318.
(13) *Aminoalkylation of Alkenes Enabled by Triple Radical Sorting | Journal of the American Chemical Society*. https://pubs.acs.org/doi/10.1021/jacs.4c14965?ref=PDF (accessed 2025-06-23).
(14) Murray, C. B.; Norris, D. J.; Bawendi, M. G. Synthesis and Characterization of Nearly Monodisperse CdE (E = Sulfur, Selenium, Tellurium) Semiconductor Nanocrystallites. *J. Am. Chem. Soc.* **1993**, *115* (19), 8706–8715. https://doi.org/10.1021/ja00072a025.
(15) Marshall, C. R.; Dvorak, J. P.; Twight, L. P.; Chen, L.; Kadota, K.; Andreeva, A. B.; Overland, A. E.; Ericson, T.; Cozzolino, A. F.; Brozek, C. K. Size-Dependent Properties of Solution-Processable Conductive MOF Nanocrystals. *J. Am. Chem. Soc.* **2022**. https://doi.org/10.1021/jacs.1c10800.
(16) An, J. M.; Franceschetti, A.; Dudiy, S. V.; Zunger, A. The Peculiar Electronic Structure of PbSe Quantum Dots. *Nano Lett.* **2006**, *6* (12), 2728–2735. https://doi.org/10.1021/nl061684x.
(17) Franceschetti, A.; Luo, J. W.; An, J. M.; Zunger, A. Origin of One-Photon and Two-Photon Optical Transitions in PbSe Nanocrystals. *Phys. Rev. B - Condens. Matter Mater. Phys.* **2009**, *79* (24), 4–7. https://doi.org/10.1103/PhysRevB.79.241311.
(18) Hosseini, M.; Keshavarz, A.; Khojaste, P. The Effect of Size Confinement on the Optical Absorption Coefficient of PbSe. *Opt. - Int. J. Light Electron Opt.* **2016**, *127* (22), 10610–10613. https://doi.org/10.1016/j.ijleo.2016.08.087.
(19) Araujo, J. J.; Brozek, C. K.; Kroupa, D. M.; Gamelin, D. R. Degenerately N-Doped Colloidal PbSe Quantum Dots: Band Assignments and Electrostatic Effects. *Nano Lett.* **2018**, *18* (6), 3893–3900. https://doi.org/10.1021/acs.nanolett.8b01235.
(20) Zheng, L.; Wei, M.; Eickemeyer, F. T.; Gao, J.; Huang, B.; Gunes, U.; Schouwink, P.; Bi, D. W.; Carnevali, V.; Mensi, M.; Biasoni, F.; Zhang, Y.; Agosta, L.; Slama, V.; Lempesis, N.; Hope, M. A.; Zakeeruddin, S. M.; Emsley, L.; Rothlisberger, U.; Pfeifer, L.; Xuan, Y.; Grätzel, M. Strain-Induced Rubidium Incorporation into Wide-Bandgap Perovskites Reduces Photovoltage Loss. *Science* **2025**, *388* (6742), 88–95. https://doi.org/10.1126/science.adt3417.
(21) Hetzl, M.; Kraut, M.; Winnerl, J.; Francaviglia, L.; Döblinger, M.; Matich, S.; Fontcuberta i Morral, A.; Stutzmann, M. Strain-Induced Band Gap Engineering in Selectively Grown GaN–(Al,Ga)N Core–Shell Nanowire Heterostructures. *Nano Lett.* **2016**, *16* (11), 7098–7106. https://doi.org/10.1021/acs.nanolett.6b03354.
(22) Santra, P.; Ghaderzadeh, S.; Ghorbani-Asl, M.; Komsa, H.-P.; Besley, E.; Krasheninnikov, A. V. Strain-Modulated Defect Engineering of Two-

Dimensional Materials. *Npj 2D Mater. Appl.* **2024**, *8* (1), 33. https://doi.org/10.1038/s41699-024-00472-x.
(23) Oliva, R.; Wozniak, T.; Faria, P. E.; Dybala, F.; Kopaczek, J.; Fabian, J.; Scharoch, P.; Kudrawiec, R. Strong Substrate Strain Effects in Multilayered $WS_2$ Revealed by High-Pressure Optical Measurements. *ACS Appl. Mater. Interfaces* **2022**, *14* (17), 19857–19868. https://doi.org/10.1021/acsami.2c01726.
(24) Davenport, A. M.; Marshall, C. R.; Nishiguchi, T.; Kadota, K.; Andreeva, A. B.; Horike, S.; Brozek, C. K. Size-Dependent Spin Crossover and Bond Flexibility in Metal–Organic Framework Nanoparticles. *J. Am. Chem. Soc.* **2024**, *146* (34), 23692–23698. https://doi.org/10.1021/jacs.4c08883.
(25) Perebeinos, V.; Chan, S.-W.; Zhang, F. 'Madelung Model' Prediction for Dependence of Lattice Parameter on Nanocrystal Size. *Solid State Commun.* **2002**, *123* (6–7), 295–297. https://doi.org/10.1016/S0038-1098(02)00266-1.
(26) Chen, B.; Penwell, D.; Benedetti, L. R.; Jeanloz, R.; Kruger, M. B. Particle-Size Effect on the Compressibility of Nanocrystalline Alumina. *Phys. Rev. B* **2002**, *66* (14), 144101. https://doi.org/10.1103/PhysRevB.66.144101.
(27) Abdullah, B. J.; Omar, M. S.; Jiang, Q. Size Dependence of the Bulk Modulus of Si Nanocrystals. *Sādhanā* **2018**, *43* (11), 174. https://doi.org/10.1007/s12046-018-0956-1.
(28) Andreeva, A. B.; Le, K. N.; Kadota, K.; Horike, S.; Hendon, C. H.; Brozek, C. K. Cooperativity and Metal–Linker Dynamics in Spin Crossover Framework Fe(1,2,3-Triazolate)2. *Chem. Mater.* **2021**, *33* (21), 8534–8545. https://doi.org/10.1021/acs.chemmater.1c03143.
(29) Grape, E. S.; Davenport, A. M.; Brozek, C. K. Dynamic Metal-Linker Bonds in Metal–Organic Frameworks. *Dalton Trans.* **2024**, *53* (5), 1935–1941. https://doi.org/10.1039/D3DT04164F.
(30) Andreeva, A. B.; Le, K. N.; Chen, L.; Kellman, M. E.; Hendon, C. H.; Brozek, C. K. Soft Mode Metal-Linker Dynamics in Carboxylate MOFs Evidenced by Variable-Temperature Infrared Spectroscopy. *J. Am. Chem. Soc.* **2020**, *142* (45), 19291–19299. https://doi.org/10.1021/jacs.0c09499.
(31) Fabrizio, K.; Lazarou, K. A.; Payne, L. I.; Twight, L. P.; Golledge, S.; Hendon, C. H.; Brozek, C. K. Tunable Band Gaps in MUV-10(M): A Family of Photoredox-Active MOFs with Earth-Abundant Open Metal Sites. *J. Am. Chem. Soc.* **2021**, *143* (32), 12609–12621. https://doi.org/10.1021/jacs.1c04808.
(32) Bunting, J. W.; Thong, K. M. Stability Constants for Some 1:1 Metal–Carboxylate Complexes. *Can. J. Chem.* **1970**, *48* (11), 1654–1656. https://doi.org/10.1139/v70-273.
(33) Fabrizio, K.; Andreeva, A. B.; Kadota, K.; Morris, A. J.; Brozek, C. K. Guest-Dependent Bond Flexibility in UiO-66, a "Stable" MOF. *Chem. Commun.* **2023**, *59* (10), 1309–1312. https://doi.org/10.1039/D2CC05895B.
(34) Fabrizio, K.; Brozek, C. K. Size-Dependent Thermal Shifts to MOF Nanocrystal Optical Gaps Induced by Dynamic Bonding. *Nano Lett.* **2023**, *23* (3), 925–930. https://doi.org/10.1021/acs.nanolett.2c04286.
(35) Scott, J. F. Soft-Mode Spectroscopy: Experimental Studies of Structural Phase Transitions. *Rev. Mod. Phys.* **1974**, *46* (1), 83–128. https://doi.org/10.1103/RevModPhys.46.83.
(36) Venkataraman, G. Soft Modes and Structural Phase Transitions. *Bull. Mater. Sci.* **1979**, *1* (3–4), 129–170. https://doi.org/10.1007/BF02743964.
(37) Brozek, C. K.; Dincă, M. Cation Exchange at the Secondary Building Units of Metal-Organic Frameworks. *Chem. Soc. Rev.* **2014**, *43* (16), 5456–5467. https://doi.org/10.1039/c4cs00002a.
(38) Brozek, C. K.; Ozarowski, A.; Stoian, S. A.; Dincă, M. Dynamic Structural Flexibility of Fe-MOF-5 Evidenced by 57 Fe Mössbauer Spectroscopy. *Inorg Chem Front* **2017**, *4* (5), 782–788. https://doi.org/10.1039/C6QI00584E.
(39) Brozek, C. K.; Dincă, M. Lattice-Imposed Geometry in Metal–Organic Frameworks: Lacunary Zn4O Clusters in MOF-5 Serve as Tripodal Chelating Ligands for Ni2+. *Chem Sci* **2012**, *3* (6), 2110–2110. https://doi.org/10.1039/c2sc20306e.
(40) Brozek, C. K.; Bellarosa, L.; Soejima, T.; Clark, T. V.; Lõpez, N.; Dincă, M. Solvent-Dependent Cation Exchange in Metal-Organic Frameworks. *Chem—Eur J* **2014**, *20*, 6871–6871. https://doi.org/10.1002/chem.201402682.
(41) Brozek, C. K.; Dincə, M. Thermodynamic Parameters of Cation Exchange in MOF-5 and MFU-4l. *Chem. Commun.* **2015**, *51* (59), 11780–11782. https://doi.org/10.1039/c5cc04249f.
(42) Brozek, C., K.; Dincă, M. Ti3+-, V2+/3+-, Cr2+/3+-, Mn2+-, and Fe2+-Subsituted MOF-5 and Redox Reactivity in Cr and Fe-MOF-5. *J. Am. Chem. Soc.* **2013**, *135*, 12886–12891. https://doi.org/10.1021/ja4064475.
(43) Leus, K.; Vandichel, M.; Liu, Y. Y.; Muylaert, I.; Musschoot, J.; Pyl, S.; Vrielinck, H.; Callens, F.; Marin, G. B.; Detavernier, C.; Wiper, P. V.; Khimyak, Y. Z.; Waroquier, M.; Van Speybroeck, V.; Van Der Voort, P. The Coordinatively Saturated Vanadium MIL-47 as a Low Leaching Heterogeneous Catalyst in the Oxidation of Cyclohexene. *J. Catal.* **2012**, *285* (1), 196–207. https://doi.org/10.1016/j.jcat.2011.09.014.
(44) Leus, K.; Muylaert, I.; Vandichel, M.; Marin, G. B.; Waroquier, M.; Van Speybroeck, V.; Van der Voort, P. The Remarkable Catalytic Activity of the Saturated Metal Organic Framework V-MIL-

47 in the Cyclohexene Oxidation. *Chem. Commun.* **2010**, *46* (28), 5085–5085. https://doi.org/10.1039/c0cc01506g.
(45) Huang, K.; Rhys, A.; Mott, N. F. Theory of Light Absorption and Non-Radiative Transitions in F-Centres. *Proc. R. Soc. Lond. Ser. Math. Phys. Sci.* **1950**, *204* (1078), 406–423. https://doi.org/10.1098/rspa.1950.0184.
(46) O'Donnell, K. P.; Chen, X. Temperature Dependence of Semiconductor Band Gaps. *Appl. Phys. Lett.* **1991**, *58* (25), 2924–2926. https://doi.org/10.1063/1.104723.
(47) Varshni, Y. P. Temperature Dependence of the Energy Gap in Semiconductors. *Physica* **1967**, *34* (1), 149–154. https://doi.org/10.1016/0031-8914(67)90062-6.
(48) Huang, J.; Davenport, A. M.; Heffernan, K.; Debela, T. T.; Marshall, C. R.; McKenzie, J.; Shen, M.; Hou, S.; Mitchell, J. B.; Ojha, K.; Hendon, C. H.; Brozek, C. K. Electrochemical Anion Sensing Using Conductive Metal–Organic Framework Nanocrystals with Confined Pores. *J. Am. Chem. Soc.* **2024**. https://doi.org/10.1021/jacs.4c06669.
(49) Huang, J.; Marshall, C. R.; Ojha, K.; Shen, M.; Golledge, S.; Kadota, K.; McKenzie, J.; Fabrizio, K.; Mitchell, J. B.; Khaliq, F.; Davenport, A. M.; LeRoy, M. A.; Mapile, A. N.; Debela, T. T.; Twight, L. P.; Hendon, C. H.; Brozek, C. K. Giant Redox Entropy in the Intercalation vs Surface Chemistry of Nanocrystal Frameworks with Confined Pores. *J. Am. Chem. Soc.* **2023**, *145* (11), 6257–6269. https://doi.org/10.1021/jacs.2c12846.
(50) Gándara, F.; Uribe-Romo, F. J.; Britt, D. K.; Furukawa, H.; Lei, L.; Cheng, R.; Duan, X.; O'Keeffe, M.; Yaghi, O. M. Porous, Conductive Metal-Triazolates and Their Structural Elucidation by the Charge-Flipping Method. *Chem. - Eur. J.* **2012**, *18* (34), 10595–10601. https://doi.org/10.1002/chem.201103433.
(51) Zhou, X.-H.; Peng, Y.-H.; Du, X.-D.; Zuo, J.-L.; You, X.-Z. Hydrothermal Syntheses and Structures of Three Novel Coordination Polymers Assembled from 1,2,3-Triazolate Ligands. **2009**. https://doi.org/10.1039/B819302A.
(52) Marshall, C. R.; Staudhammer, S. A.; Brozek, C. K. Size Control over Metal-Organic Framework Porous Nanocrystals. *Chem. Sci.* **2019**, *10* (41), 9396–9408. https://doi.org/10.1039/c9sc03802g.
(53) Fabrizio, K.; L. Gormley, E.; M. Davenport, A.; H. Hendon, C.; K. Brozek, C. Gram-Scale Synthesis of MIL-125 Nanoparticles and Their Solution Processability. *Chem. Sci.* **2023**. https://doi.org/10.1039/D3SC02257A.
(54) Marshall, C. R.; Timmel, E. E.; Staudhammer, S. A.; Brozek, C. K. Experimental Evidence for a General Model of Modulated MOF Nanoparticle Growth. *Chem. Sci.* **2020**, *11* (42), 11539–11547. https://doi.org/10.1039/d0sc04845c.
(55) Cravillon, J.; Nayuk, R.; Springer, S.; Feldhoff, A.; Huber, K.; Wiebcke, M. Controlling Zeolitic Imidazolate Framework Nano- and Microcrystal Formation: Insight into Crystal Growth by Time-Resolved In Situ Static Light Scattering. *Chem. Mater.* **2011**, *23* (8), 2130–2141. https://doi.org/10.1021/cm103571y.
(56) Cravillon, J.; Münzer, S.; Lohmeier, S.-J.; Feldhoff, A.; Huber, K.; Wiebcke, M. Rapid Room-Temperature Synthesis and Characterization of Nanocrystals of a Prototypical Zeolitic Imidazolate Framework. *Chem. Mater.* **2009**, *21* (8), 1410–1412. https://doi.org/10.1021/cm900166h.
(57) Lim, I. H.; Schrader, W.; Schüth, F. Insights into the Molecular Assembly of Zeolitic Imidazolate Frameworks by ESI-MS. *Chem. Mater.* **2015**, *27* (8), 3088–3095. https://doi.org/10.1021/acs.chemmater.5b00614.
(58) Li, Y.; Wang, K.; Zhou, W.; Li, Y.; Vila, R.; Huang, W.; Wang, H.; Chen, G.; Wu, G.-H.; Tsao, Y.; Wang, H.; Sinclair, R.; Chiu, W.; Cui, Y. Cryo-EM Structures of Atomic Surfaces and Host-Guest Chemistry in Metal-Organic Frameworks. *Matter* **2019**, *1* (2), 428–438. https://doi.org/10.1016/j.matt.2019.06.001.
(59) Liu, X.; Chee, S. W.; Raj, S.; Sawczyk, M.; Král, P.; Mirsaidov, U. Three-Step Nucleation of Metal–Organic Framework Nanocrystals. *Proc. Natl. Acad. Sci.* **2021**, *118* (10), e2008880118. https://doi.org/10.1073/pnas.2008880118.
(60) LeRoy, M. A.; Perera, A. S.; Lamichhane, S.; Mapile, A. N.; Khaliq, F.; Kadota, K.; Zhang, X.; Ha, S.; Fisher, R.; Wu, D.; Risko, C.; Brozek, C. K. Colloidal Stability and Solubility of Metal–Organic Framework Particles. *Chem. Mater.* **2024**, *36* (8), 3673–3682. https://doi.org/10.1021/acs.chemmater.3c03191.
(61) Mapile, A. N.; Svensson Grape, E.; Brozek, C. K. Solvation of Nanoscale Materials. *Chem. Mater.* **2024**. https://doi.org/10.1021/acs.chemmater.4c01518.
(62) Kaur, S.; Lesea-Pringle, B.; Marjit, S.; Hong, H.; Rahman, A.; Ma, B.; Favaro, D. C.; DelRe, C. Simple Strategies to Quantify and Control Polymer Threading into Micropores. *J. Am. Chem. Soc.* **2025**, *147* (25), 22245–22252. https://doi.org/10.1021/jacs.5c07556.
(63) DelRe, C.; Hong, H.; Jiménez-Ángeles, F.; Wenny, M. B.; Erdosy, D. P.; Cho, J.; Britt, S.; Olvera de la Cruz, M.; Mason, J. A. Protein Coatings Dictate the Dispersibility and Stability of Hydrophobic Zeolitic-Imidazolate Frameworks in Water. *J. Phys. Chem. B* **2025**, *129* (11), 3120–3130. https://doi.org/10.1021/acs.jpcb.5c00972.
(64) DelRe, C.; Hong, H.; Wenny, M. B.; Erdosy, D. P.; Cho, J.; Lee, B.; Mason, J. A. Design

Principles for Using Amphiphilic Polymers To Create Microporous Water. *J. Am. Chem. Soc.* **2023**, *145* (36), 19982–19988. https://doi.org/10.1021/jacs.3c06627.
(65) Park, S. V.; Bhai, L.; Lee, G. A.; Park, A.-H. A.; Marbella, L. E.; Owen, J. S. Steric Stabilization of Colloidal UiO-66 Nanocrystals with Oleylammonium Octadecylphosphonate. September 25, 2024. https://doi.org/10.26434/chemrxiv-2024-8kh7m.
(66) Mapile, A. N.; LeRoy, M. A.; Fabrizio, K.; Scatena, L. F.; Brozek, C. K. The Surface of Colloidal Metal–Organic Framework Nanoparticles Revealed by Vibrational Sum Frequency Scattering Spectroscopy. *ACS Nano* **2024**, *18* (20), 13406–13414. https://doi.org/10.1021/acsnano.4c03758.
(67) Osborne, S. J.; Wellens, S.; Ward, C.; Felton, S.; Bowman, R. M.; Binnemans, K.; Swadźba-Kwaśny, M.; Gunaratne, H. Q. N.; Nockemann, P. Thermochromism and Switchable Paramagnetism of Cobalt( II ) in Thiocyanate Ionic Liquids. *Dalton Trans.* **2015**, *44* (25), 11286–11289. https://doi.org/10.1039/C5DT01829C.
(68) Park, J. G.; Aubrey, M. L.; Oktawiec, J.; Chakarawet, K.; Darago, L. E.; Grandjean, F.; Long, G. J.; Long, J. R. Charge Delocalization and Bulk Electronic Conductivity in the Mixed-Valence Metal–Organic Framework Fe(1,2,3-Triazolate)2(BF4)x. *J. Am. Chem. Soc.* **2018**, *140* (27), 8526–8534. https://doi.org/10.1021/jacs.8b03696.
(69) Park, J. G.; Collins, B. A.; Darago, L. E.; Runčevski, T.; Ziebel, M. E.; Aubrey, M. L.; Jiang, H. Z. H.; Velasquez, E.; Green, M. A.; Goodpaster, J. D.; Long, J. R. Magnetic Ordering through Itinerant Ferromagnetism in a Metal–Organic Framework. *Nat. Chem.* **2021**, *13* (6), 594–598. https://doi.org/10.1038/s41557-021-00666-6.
(70) Jørgensen, Chr. K. Chemical Bonding Inferred from Visible and Ultraviolet Absorption Spectra. In *Solid State Physics*; Elsevier, 1962; Vol. 13, pp 375–462. https://doi.org/10.1016/S0081-1947(08)60460-9.
(71) Li, K.; Xue, D. Estimation of Electronegativity Values of Elements in Different Valence States. *J. Phys. Chem. A* **2006**, *110* (39), 11332–11337. https://doi.org/10.1021/jp062886k.
(72) Yang, Y.; Zhao, X.; Liang, J.; Yang, Q.; Zhang, T.; Wang, Y.; Yang, X.; Zou, B. Pressure-Promoted Self-Trapped Exciton Emission and White-Light Harvesting in Lead Halide Metal–Organic Frameworks at Ambient Conditions. *Laser Photonics Rev.* **2025**, *19* (10), 2401961. https://doi.org/10.1002/lpor.202401961.
(73) Ma, W.; Song, X.; Yin, J.; Fei, H. Intrinsic Self-Trapped Broadband Emission from Zinc Halide-Based Metal–Organic Frameworks. *Chem. Commun.* **2021**, *57* (11), 1396–1399. https://doi.org/10.1039/D0CC07320B.
(74) De Paula, A. M.; Li, S.; Hou, B.; Vadivel, S.; Teles-Ferreira, D. C.; Iudica, A.; Kabacinski, P.; Hosseini, H.; McArthur, J.; Cerullo, G.; Qiu, D. Y.; Guo, P.; Camargo, F. V. A. Time-Domain Observation of Ultrafast Self-Trapped Exciton Formation in Lead-Free Double Halide Perovskites. *J. Am. Chem. Soc.* **2025**, jacs.5c06628. https://doi.org/10.1021/jacs.5c06628.
(75) Gu, Y.-P.; Cui, R.; Zhang, Z.-L.; Xie, Z.-X.; Pang, D.-W. Ultrasmall Near-Infrared $Ag_2$ Se Quantum Dots with Tunable Fluorescence for *in Vivo* Imaging. *J. Am. Chem. Soc.* **2012**, *134* (1), 79–82. https://doi.org/10.1021/ja2089553.
(76) Shi, Y.; Wang, Z.; Meng, T.; Yuan, T.; Ni, R.; Li, Y.; Li, X.; Zhang, Y.; Tan, Z.; Lei, S.; Fan, L. Red Phosphorescent Carbon Quantum Dot Organic Framework-Based Electroluminescent Light-Emitting Diodes Exceeding 5% External Quantum Efficiency. *J. Am. Chem. Soc.* **2021**, *143* (45), 18941–18951. https://doi.org/10.1021/jacs.1c07054.
(77) Weiss, E. A.; Chiechi, R. C.; Geyer, S. M.; Porter, V. J.; Bell, D. C.; Bawendi, M. G.; Whitesides, G. M. Size-Dependent Charge Collection in Junctions Containing Single-Size and Multi-Size Arrays of Colloidal CdSe Quantum Dots. *J. Am. Chem. Soc.* **2008**, *130* (1), 74–82. https://doi.org/10.1021/ja076438h.
(78) Frederick, M. T.; Amin, V. a; Swenson, N. K.; Ho, A. Y.; Weiss, E. a. Control of Exciton Confinement in Quantum Dot–Organic Complexes through Energetic Alignment of Interfacial Orbitals. *Nano Lett.* **2013**, *13* (1), 287–292. https://doi.org/10.1021/nl304098e.
(79) Frederick, M. T.; Amin, V. a.; Weiss, E. a. Optical Properties of Strongly Coupled Quantum Dot-Ligand Systems. *J. Phys. Chem. Lett.* **2013**, *4* (4), 634–640. https://doi.org/10.1021/jz301905n.
(80) Frederick, M. T.; Amin, V. A.; Swenson, N. K.; Ho, A. Y.; Weiss, E. A. Control of Exciton Confinement in Quantum Dot–Organic Complexes through Energetic Alignment of Interfacial Orbitals. *Nano Lett.* **2013**, *13* (1), 287–292. https://doi.org/10.1021/nl304098e.
(81) Gutmann, V. Solvent Effects on the Reactivities of Organometallic Compounds. *Coord. Chem. Rev.* **1976**, *18* (2), 225–255. https://doi.org/10.1016/S0010-8545(00)82045-7.
(82) Svensson Grape, E.; Davenport, A. M.; Kadota, K.; Horike, S.; Brozek, C. K. Crystallographic Evidence of Size-Dependent Bond Flexibility in Metal–Organic Framework Nanocrystals. *ACS Mater. Lett.* **2025**, 3893–3900. https://doi.org/10.1021/acsmaterialslett.5c01070.
(83) Li, J.; Shan, Z.; Ma, E. Elastic Strain Engineering for Unprecedented Materials Properties. *MRS*

*Bull.* **2014**, *39* (2), 108–114. https://doi.org/10.1557/mrs.2014.3.
(84) Andrade, A. B.; Ferreira, N. S.; Valerio, M. E. G. Particle Size Effects on Structural and Optical Properties of $BaF_2$ Nanoparticles. *RSC Adv.* **2017**, *7* (43), 26839–26848. https://doi.org/10.1039/C7RA01582H.
(85) Mocherla, P. S. V.; Sahana, M. B.; Gopalan, R.; Ramachandra Rao, M. S.; Nanda, B. R. K.; Sudakar, C. Microstrain Engineered Magnetic Properties in $Bi_{1-x}Ca_xFe_{1-y}Ti_yO_{3-\delta}$ Nanoparticles: Deviation from Néel's 1/ *d* Size-Dependent Magnetization Behaviour. *Mater. Res. Express* **2017**, *4* (10), 106106. https://doi.org/10.1088/2053-1591/aa9088.
(86) Qin, W.; Nagase, T.; Umakoshi, Y.; Szpunar, J. A. Relationship between Microstrain and Lattice Parameter Change in Nanocrystalline Materials. *Philos. Mag. Lett.* **2008**, *88* (3), 169–179. https://doi.org/10.1080/09500830701840155.
(87) Bardeen, J.; Shockley, W. Deformation Potentials and Mobilities in Non-Polar Crystals. *Phys. Rev.* **1950**, *80* (1), 72–80. https://doi.org/10.1103/PhysRev.80.72.
(88) Ghosh, A.; Ahmed, F.; Ferdous, Md. J.; Juhi, Mst. M. J.; Buian, M. F. I.; Miazee, A. A.; Sajid, M.; Maniruzzaman, Md.; Tighezza, A. M.; Ahmmed, M. F.; Islam, Md. S. Strain-Induced Changes in the Electronic, Optical and Mechanical Properties of the Inorganic Cubic Halide Perovskite Sr3PBr3 with FP-DFT. *J. Phys. Chem. Solids* **2024**, *191*, 112053. https://doi.org/10.1016/j.jpcs.2024.112053.
(89) Tahini, H.; Chroneos, A.; Grimes, R. W.; Schwingenschlögl, U.; Dimoulas, A. Strain-Induced Changes to the Electronic Structure of Germanium. *J. Phys. Condens. Matter* **2012**, *24* (19), 195802. https://doi.org/10.1088/0953-8984/24/19/195802.
(90) Hetzl, M.; Kraut, M.; Winnerl, J.; Francaviglia, L.; Döblinger, M.; Matich, S.; Fontcuberta I Morral, A.; Stutzmann, M. Strain-Induced Band Gap Engineering in Selectively Grown GaN–(Al,Ga)N Core–Shell Nanowire Heterostructures. *Nano Lett.* **2016**, *16* (11), 7098–7106. https://doi.org/10.1021/acs.nanolett.6b03354.
(91) Feng, J.; Qian, X.; Huang, C.-W.; Li, J. Strain-Engineered Artificial Atom as a Broad-Spectrum Solar Energy Funnel. *Nat. Photonics* **2012**, *6* (12), 866–872. https://doi.org/10.1038/nphoton.2012.285.
(92) Roldán, R.; Castellanos-Gomez, A.; Cappelluti, E.; Guinea, F. Strain Engineering in Semiconducting Two-Dimensional Crystals. *J. Phys. Condens. Matter* **2015**, *27* (31), 313201. https://doi.org/10.1088/0953-8984/27/31/313201.
(93) Carrascoso, F.; Li, H.; Frisenda, R.; Castellanos-Gomez, A. Strain Engineering in Single-, Bi- and Tri-Layer MoS2, MoSe2, WS2 and WSe2. *Nano Res.* **2021**, *14* (6), 1698–1703. https://doi.org/10.1007/s12274-020-2918-2.
(94) Conley, H. J.; Wang, B.; Ziegler, J. I.; Haglund, R. F.; Pantelides, S. T.; Bolotin, K. I. Bandgap Engineering of Strained Monolayer and Bilayer $MoS_2$. *Nano Lett.* **2013**, *13* (8), 3626–3630. https://doi.org/10.1021/nl4014748.
(95) Fabrizio, K.; Brozek, C. K. Size-Dependent Thermal Shifts to MOF Nanocrystal Optical Gaps Induced by Dynamic Bonding. *Nano Lett.* **2023**, *23* (3), 925–930. https://doi.org/10.1021/acs.nanolett.2c04286.
(96) Zhu, M.; Xu, D.; Ouyang, Y.; Zhang, H.; Liu, L.; Meng, J.; Xiao, S.; Chen, Z.; He, J. Strain-Mediated Second Harmonic Generation Enhancement of Bimetallic Metal–Organic Frameworks. *J. Phys. Chem. Lett.* **2024**, *15* (49), 12120–12128. https://doi.org/10.1021/acs.jpclett.4c02915.
(97) Yue, X.; Cheng, L.; Li, F.; Fan, J.; Xiang, Q. Highly Strained Bi-MOF on Bismuth Oxyhalide Support with Tailored Intermediate Adsorption/Desorption Capability for Robust $CO_2$ Photoreduction. *Angew. Chem. Int. Ed.* **2022**, *61* (40), e202208414. https://doi.org/10.1002/anie.202208414.
(98) Yan, Y.; Wang, C.; Cai, Z.; Wang, X.; Xuan, F. Tuning Electrical and Mechanical Properties of Metal–Organic Frameworks by Metal Substitution. *ACS Appl. Mater. Interfaces* **2023**, *15* (36), 42845–42853. https://doi.org/10.1021/acsami.3c08470.
(99) Yeung, H. H.-M.; Yoshikawa, G.; Minami, K.; Shiba, K. Strain-Based Chemical Sensing Using Metal–Organic Framework Nanoparticles. *J. Mater. Chem. A* **2020**, *8* (35), 18007–18014. https://doi.org/10.1039/D0TA07248F.
(100) Stojković, M.; Pašti, I. A. Strain Engineering for Tuning the Photocatalytic Activity of Metal-Organic Frameworks-Theoretical Study of the UiO-66 Case. *Catalysts* **2021**, *11* (2), 264. https://doi.org/10.3390/catal11020264.
(101) Taddei, M.; Schukraft, G. M.; Warwick, M. E. A.; Tiana, D.; McPherson, M. J.; Jones, D. R.; Petit, C. Band Gap Modulation in Zirconium-Based Metal–Organic Frameworks by Defect Engineering. *J. Mater. Chem. A* **2019**, *7* (41), 23781–23786. https://doi.org/10.1039/C9TA05216J.
(102) Schmieder, P.; Denysenko, D.; Grzywa, M.; Baumgärtner, B.; Senkovska, I.; Kaskel, S.; Sastre, G.; Van Wüllen, L.; Volkmer, D. CFA-1: The First Chiral Metal–Organic Framework Containing Kuratowski-Type Secondary Building Units. *Dalton Trans.* **2013**, *42* (30), 10786. https://doi.org/10.1039/c3dt50787d.
(103) Ye, J.; Gagliardi, L.; Cramer, C. J.; Truhlar, D. G. Computational Screening of MOF-Supported Transition Metal Catalysts for Activity and

Selectivity in Ethylene Dimerization. *J. Catal.* **2018**, *360*, 160–167. https://doi.org/10.1016/j.jcat.2017.12.007.
(104) Ortega, D. E.; Matute, R. A. Influence of Linkers on the Kuratowski-Type Secondary Building Unit in Nickel Single-Site MOFs for Ethylene Oligomerization Catalysis: A Computational Study. *Catal. Sci. Technol.* **2021**, *11* (7), 2422–2432. https://doi.org/10.1039/D0CY02137G.
(105) Becke, A. D. Density-Functional Thermochemistry. III. The Role of Exact Exchange. *J. Chem. Phys.* **1993**, *98* (7), 5648–5652. https://doi.org/10.1063/1.464913.
(106) Lee, C.; Yang, W.; Parr, R. G. Development of the Colle-Salvetti Correlation-Energy Formula into a Functional of the Electron Density. *Phys. Rev. B* **1988**, *37* (2), 785–789. https://doi.org/10.1103/PhysRevB.37.785.
(107) Miehlich, B.; Savin, A.; Stoll, H.; Preuss, H. Results Obtained with the Correlation Energy Density Functionals of Becke and Lee, Yang and Parr. *Chem. Phys. Lett.* **1989**, *157* (3), 200–206. https://doi.org/10.1016/0009-2614(89)87234-3.
(108) Schautz, F.; Flad, H.-J.; Dolg, M. Quantum Monte Carlo Study of Be 2 and Group 12 Dimers M 2 (M = Zn, Cd, Hg). *Theor. Chem. Acc. Theory Comput. Model. Theor. Chim. Acta* **1998**, *99* (4), 231–240. https://doi.org/10.1007/s002140050331.
(109) M. J. Frisch, G. W. Trucks, H. B. Schlegel, G. E. Scuseria, M. A. Robb, J. R. Cheeseman, G. Scalmani, V. Barone, G. A. Petersson, H. Nakatsuji, X. Li, M. Caricato, A. V. Marenich, J. Bloino, B. G. Janesko, R. Gomperts, B. Mennucci, H. P. Hratchian, J. V. Ortiz, A. F. Izmaylov, J. L. Sonnenberg, D. Williams-Young, F. Ding, F. Lipparini, F. Egidi, J. Goings, B. Peng, A. Petrone, T. Henderson, D. Ranasinghe, V. G. Zakrzewski, J. Gao, N. Rega, G. Zheng, W. Liang, M. Hada, M. Ehara, K. Toyota, R. Fukuda, J. Hasegawa, M. Ishida, T. Nakajima, Y. Honda, O. Kitao, H. Nakai, T. Vreven, K. Throssell, J. A. Montgomery, Jr., J. E. Peralta, F. Ogliaro, M. J. Bearpark, J. J. Heyd, E. N. Brothers, K. N. Kudin, V. N. Staroverov, T. A. Keith, R. Kobayashi, J. Normand, K. Raghavachari, A. P. Rendell, J. C. Burant, S. S. Iyengar, J. Tomasi, M. Cossi, J. M. Millam, M. Klene, C. Adamo, R. Cammi, J. W. Ochterski, R. L. Martin, K. Morokuma, O. Farkas, J. B. Foresman, and D. J. Fox, Gaussian, Inc.,. 16 :Gaussian 16, Revision B.01, Wallingford CT, 2016. **2016**.
(110) Balzar, D. Voigt Function Model in Diffraction-Line Broadening Analysis. In *Defect and Microstructure Analysis by Diffraction*; Oxford University PressOxford, 2000; pp 94–126. https://doi.org/10.1093/oso/9780198501893.003.0007.
(111) Balzar, D.; Audebrand, N.; Daymond, M. R.; Fitch, A.; Hewat, A.; Langford, J. I.; Le Bail, A.; Louër, D.; Masson, O.; McCowan, C. N.; Popa, N. C.; Stephens, P. W.; Toby, B. H. Size–Strain Line-Broadening Analysis of the Ceria Round-Robin Sample. *J. Appl. Crystallogr.* **2004**, *37* (6), 911–924. https://doi.org/10.1107/S0021889804022551.
(112) Coelho, A. TOPAS-Academic V5, Coelho Software. **2012**.
(113) Yang, B.; Bogachuk, D.; Suo, J.; Wagner, L.; Kim, H.; Lim, J.; Hinsch, A.; Boschloo, G.; Nazeeruddin, M. K.; Hagfeldt, A. Strain Effects on Halide Perovskite Solar Cells. *Chem. Soc. Rev.* **2022**, *51* (17), 7509–7530. https://doi.org/10.1039/D2CS00278G.
(114) Conley, H. J.; Wang, B.; Ziegler, J. I.; Haglund, R. F.; Pantelides, S. T.; Bolotin, K. I. Bandgap Engineering of Strained Monolayer and Bilayer $MoS_2$. *Nano Lett.* **2013**, *13* (8), 3626–3630. https://doi.org/10.1021/nl4014748.
(115) Balaghi, L.; Bussone, G.; Grifone, R.; Hübner, R.; Grenzer, J.; Ghorbani-Asl, M.; Krasheninnikov, A. V.; Schneider, H.; Helm, M.; Dimakis, E. Widely Tunable GaAs Bandgap via Strain Engineering in Core/Shell Nanowires with Large Lattice Mismatch. *Nat. Commun.* **2019**, *10* (1), 2793. https://doi.org/10.1038/s41467-019-10654-7.
(116) Svensson Grape, E.; Davenport, A.; Kadota, K.; Horike, S.; Brozek, C. Crystallographic Evidence of Size-Dependent Bond Flexibility in MOF Nanocrystals. Chemistry July 25, 2025. https://doi.org/10.26434/chemrxiv-2025-4xf5x.
(117) Prestipino, C.; Regli, L.; Vitillo, J. G.; Bonino, F.; Damin, A.; Lamberti, C.; Zecchina, A.; Solari, P. L.; Kongshaug, K. O.; Bordiga, S. Local Structure of Framework Cu(II) in HKUST-1 Metallorganic Framework: Spectroscopic Characterization upon Activation and Interaction with Adsorbates. *Chem. Mater.* **2006**, *18* (5), 1337–1346. https://doi.org/10.1021/cm052191g.
(118) Kim, H. K.; Yun, W. S.; Kim, M.-B.; Kim, J. Y.; Bae, Y.-S.; Lee, J.; Jeong, N. C. A Chemical Route to Activation of Open Metal Sites in the Copper-Based Metal–Organic Framework Materials HKUST-1 and Cu-MOF-2. *J. Am. Chem. Soc.* **2015**, *137* (31), 10009–10015. https://doi.org/10.1021/jacs.5b06637.
(119) Bhunia, M. K.; Hughes, J. T.; Fettinger, J. C.; Navrotsky, A. Thermochemistry of Paddle Wheel MOFs: Cu-HKUST-1 and Zn-HKUST-1. *Langmuir* **2013**, *29* (25), 8140–8145. https://doi.org/10.1021/la4012839.
(120) Irandoost, E.; Farsi, H.; Farrokhi, A.; Barekati, N. S.; Li, Z. Environmentally Benign Synthesis of Copper Benzenetricarboxylic Acid MOF as an Electrocatalyst for Overall Water Splitting and $CO_2$ Reduction. *ECS Adv.* **2022**, *1* (2), 020501. https://doi.org/10.1149/2754-2734/ac6ad5.

(121) Ross, P. K.; Allendorf, M. D.; Solomon, E. I. Detailed Spectral Studies of Copper Acetate: Excited-State Interactions in Copper Dimers. *J. Am. Chem. Soc.* **1989**, *111* (11), 4009–4021. https://doi.org/10.1021/ja00193a038.